THE FLUORESCENCE OF RARE EARTH IONS IN ALKALI HALIDES

THE FLUORESCENCE OF RARE EARTH IONS IN ALKALI HALIDES

by

MARGARET ANN BUCHANAN, B.Sc.

A Thesis
Submitted to the Faculty of Graduate Studies
in Partial Fulfilment of the Requirements
for the Degree
Doctor of Philosophy

McMaster University
October 1969

DOCTOR OF PHILOSOPHY (1969)
(Physics)

McMASTER UNIVERSITY
Hamilton, Ontario.

TITLE: The Fluorescence of Rare Earth Ions in Alkali Halides

AUTHOR: Margaret Ann Buchanan, B.Sc., (University of Manitoba)

SUPERVISOR: Dr. T. Timusk

NUMBER OF PAGES: vi, 91

SCOPE AND CONTENTS:

High resolution fluorescence spectra are presented of the sideband of the $^5D_0 \rightarrow {}^7F_0$ transition of Sm^{++} in KBr and KCl. Several Van Hove singularities of the phonon spectrum of the host material are directly observed. They occur at slightly different frequencies from those predicted by density of states calculations based on neutron diffraction measurements. Numerical calculations of both sidebands are given and compared with experiment, with quite good agreement. Sidebands observed for Eu^{++} in KBr and KCl are also presented and discussed.

ACKNOWLEDGEMENTS

I am grateful to my supervisor, Dr. T. Timusk, for his guidance and help throughout the course of this research, and to Dr. E. J. Woll and Dr. J. P. Carbotte for their guidance on the theoretical aspect of this work.

This work was supported by a grant from the National Research Council of Canada. I wish to thank them also for personal financial support.

TABLE OF CONTENTS

LIST OF FIGURES

CHAPTER 1

INTRODUCTION

The spectra of ions in crystals have been the subject of extensive experimental and theoretical studies for many years (see,for example, Ballhausen, 1962,or the review article by McClure, 1959). This work has given information on the observed sharp lines, arising from electronic transitions of the impurity ions, and about the bands which often accompany these lines. These bands are characteristic of the vibrations of the lattice, and of the interaction of the lattice with the impurity ion. While the analysis of the optic absorption and emission processes in systems where the electronic and lattice states are strongly coupled is very difficult, the situation where the impurity ion electronic levels are strongly localized and the coupling to the lattice weak presents a much simpler problem. An example of this is the case of the rare-earth ions, where the f wave functions are localized and the electronic levels of these ions in crystals are found to be similar to those of the free ion. The weak interaction, in turn, gives rise to lattice vibrational sidebands for which it is easier to describe and interpret the mechanism of coupling.

While progress has been made on the problem of the electronic levels in recent years, the part of the problem related to the lattice vibrations is less well understood. Coupling mechanisms have been discussed and calculations on simplified models of the lattice have been made; however, no detailed calculations on realistic models exist. Thus, a choice of the mechanism responsible for the electron-lattice coupling cannot be made.

In this thesis, such a calculation for a vibrational sideband is made. The system considered is that of a divalent rare-earth ion replacing an alkali ion in an alkali-halide lattice. This system is especially suitable for the study of vibrational sidebands of electronic transitions for several reasons. First, there is a considerable background of work on the electronic levels of this system (Kaplyanskii and Feofilov 1964, Bron and Heller 1964, Fong and Wong 1967). Secondly, the vibrational modes of the pure lattice have been measured by inelastic neutron scattering, and a fairly reliable model is available for interpolation between the neutron measurements.

Kaplyanskii and Feofilov (1964) first studied the absorption and fluorescence of various divalent samarium-alkali halide systems at liquid helium temperatures. In absorption they observed a series of intense vibrational bands which they associated with the allowed transitions of the Sm^{++} ion from $4f^6$ to $4f^5 5d$ levels. In luminescence, however, the transitions giving rise to the sharp electronic lines observed appeared to be the forbidden transitions between the levels of the $4f^6$ configuration. Similar vibrational frequencies were observed in both absorption and emission spectra, with the exception of the sideband on the long wavelength side of the ${}^5D_0 \rightarrow {}^7F_0$ transition line. This sideband is not dominated by a single frequency, but instead has a structured continuum extending over the range of the one-phonon lattice spectrum.

This sideband has also been studied by Bron (1965) and he has suggested a mechanism for the coupling between lattice modes and the rare-earth ion. This mechanism will be discussed in Appendix C. His mechanism depends on there being a strong field at the Sm^{++} site due to the presence of a K^+ vacancy (to compensate for the double charge of the impurity ion) at the second neighbour site $(\frac{a}{2},\frac{a}{2},0)$. This assumption is based on the work of Bron and Heller (1964). They attempted to show that the emission lines were associated with transitions from the ${}^5D_0$ level to the ${}^7F_J$ levels, allowed by a vacancy in this position, by calculating the crystal field splittings of the levels on a point charge model. Fairly good agreement with the measured splittings was found.

However, more recently, Fong and Wong (1967) studied the system again, pointing out that in the fluorescence spectrum identified by Bron and Heller as Stark splitting of the $^7F_1$ and $^7F_2$ levels, the splitting is equal and so appears more like vibronic lines than Stark components; and also that Bron and Heller considered only one C_{2v} site for the vacancy. Fong and Wong then studied the emission spectrum using the Zeeman effect, and they concluded, by comparison with calculated Zeeman patterns, that there were four different kinds of Sm^{++}:K^+-vacancy pairs with C_{4v} symmetry, probably corresponding to different distances of separation between rare-earth ion and compensating vacancy; and, from their study of the $^7F_5$ lines which did indicate C_{2v} symmetry, they concluded that the K^+ vacancy was sufficiently far from the rare-earth ion that the immediate environment of the Sm^{++} was still cubic.

Thus, Bron's assumption of a strong vacancy field may not be good, and the symmetry of the defect site may be higher than C_{2v}.

The aim of the work presented in this thesis was to study further the sidebands of the $^5D_0 \rightarrow {}^7F_0$ luminescence with higher resolution to reveal Van Hove singularities in the phonon spectra and to verify a model of the interaction of the host lattice with the rare-earth impurity ion by numerical calculations, making use of the extensive measurements of phonon dispersion curves for alkali halides by neutron diffraction and calculations of phonon densities of states by various authors.

In Chapter 2, the experimental methods are discussed and high resolution spectra taken at 7°K of the phonon sidebands of the $^5D_0 \rightarrow {}^7F_0$ transition in luminescence are presented for KBr:Sm^{++} and KCl:Sm^{++}; luminescence spectra of the phonon sidebands above 4105 Å for europium-doped KBr and KCl are also given. Chapter 3 introduces the notation used and reviews the background theory. In Chapter 4 a theoretical mechanism for the samarium sidebands is presented, and the results of numerical calculations are given and compared with experimental curves. In Chapter 5, a discussion of similar sidebands such as europium-doped KBr and KCl or CaF_2:Sm^{++} sidebands is given .

CHAPTER 2

EXPERIMENTAL WORK

A. Experimental methods

The crystals were grown by the Kyropoulos method in an airtight Vycor chamber. Glazed porcelain crucibles were used. Metal parts of the apparatus were made of Inconel, which proved to be unattacked by the hot salt. The chamber was evacuable, with provision for the admittance of inert or reducing atmospheres.

Reagent grade alkali halides from Fisher Scientific were used, with an additive doping of less than 0.1 at.% of anhydrous $SmCl_3$ supplied by American Potash.

The mixture was dried under vacuum for two hours at a temperature of 90°C. High purity hydrogen was then admitted. Throughout the rest of the growing procedure, an atmosphere of hydrogen at slightly above atmospheric pressure was maintained in the chamber; a slow flow was permitted to carry off impurities and vapourized salt. The mixture was raised to the melting point and held there for two hours to reduce the samarium dopant to the divalent state. Any remaining undissolved impurities were then lifted out of the melt with a pyrex "foot". By this stage, the melt had changed from being colourless to a deep red.

A boule of about 1-1/4" diameter and up to 2" in length was then pulled from the melt over a four hour period. More rapid growth resulted in heavily strained and distorted crystals. The resultant boules were purple in colour. Sample crystals of about 5/8"×3/8"×1/8" were cleaved from these boules. Analysis by wet chemistry showed the samples to contain less than .01 at.% samarium.

$SmBr_3$ was also used as a dopant for KBr. This was obtained from the $SmCl_3$ by adding an excess of ammonium carbonate to $SmCl_3$ dissolved in water, and then treating the resultant precipitate with hydrobromic acid. This solution was then dried slowly below 100°C, and the resulting dark-brown crystals used as dopant.

Europium-doped crystals of KBr and KCl were grown in the same way using $EuCl_3$ from the same source; again, KBr crystals were also doped with $EuBr_3$.

Samples were quenched from 25° below the melting point immediately before use to dissolve rare-earth aggregates (Bron and Heller 1964), by dropping into oil. Spectra were taken of both quenched and unquenched samples.

The samples were mounted in a metal helium dewar, such that the fluorescence could be detected at right angles to the exciting light. The temperature of the sample could be determined with a germanium resistance thermometer mounted on the sample-holder and a gold-.02% iron vs. copper differential thermocouple from the resistance thermometer to the sample itself.

The luminescence was excited with an Osram HBO 500W high pressure mercury lamp. A saturated $CuSO_4$ solution was used as a filter in the exciting beam and a red filter with a cutoff at 6500 Å in the output fluorescence beam. With this combination of filters no detectable light from the lamp reached the spectrometer.

A Spex 3/4 meter Czerny-Turner spectrometer with 2" curved slits was used. It was fitted with a 10 cm grating blazed for 5000 Å, with 1200 ℓ/mm. The resolution of the spectrometer was 0.2 cm^{-1} as determined from the half-width of the 3131 Å mercury doublet, with slit height 10 mm and width 12 μ. This slit width and height were typical of those used. Aspheric lenses were used to image on the crystal and the slit.

A red sensitive photomultiplier (R-136) supplied by the Hamamatsu TV Company was used for detecting the luminescence. The response of the system of red filter, spectrometer, and photomultiplier was determined using a standard tungsten light source. The response throughout the range is shown in figure 1.

Figure 1. The relative response of the system of photomultiplier spectrometer, and red filter, in the region from 6850 Å to 7050 Å, normalized to unity at 6850 Å. The units are photons/unit wavelength. The one-phonon regions for KBr:Sm^{++} and KCl:Sm^{++} are indicated.

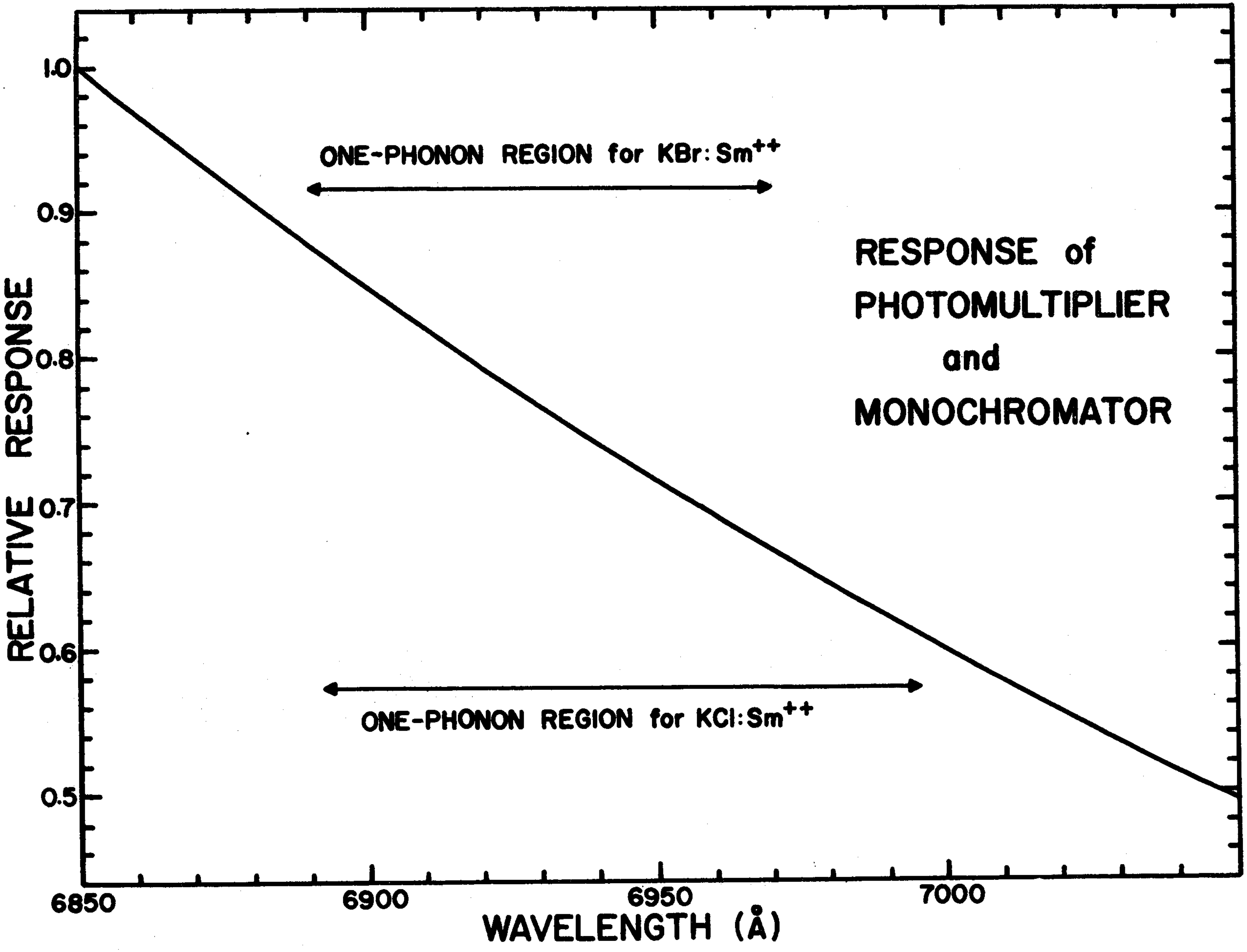ONE-PHONON REGION for KBr:Sm++
RESPONSE of PHOTOMULTIPLIER and MONOCHROMATOR
ONE-PHONON REGION for KCl:Sm++
RELATIVE RESPONSE
1.0
0.9
0.8
0.7
0.6
0.5
6850
6900
6950
7000
WAVELENGTH (Å)

For the fluorescence spectra of Eu^{++} in alkali halides, a Corning #584 glass filter was used in the input beam, as well as a diluted $CuSO_4$ solution. No filter was used in the output beam; however, no detectable radiation from the lamp was observed in the region from 4000 Å to 4350 Å.

Typical scanning speed was 2 Å/min. The output of the photomultiplier was fed directly to the pen recorder.

B. Experimental results

The fluorescence sidebands of Sm^{++} in KBr and KCl at 7°K are presented in figures 2 and 3. The origin of the frequency scale in each case is the electronic transition (zero-phonon line) which occurs at 6890.4 Å for Sm^{++}:KBr and at 6892.0 Å for Sm^{++}:KCl (Kaplyanskii and Feofilov 1964). This line is broadened or split, depending on the concentration of impurities and the quenching of the crystal; the sidebands, however, are unchanged from sample to sample.

The line width of the zero-phonon line in KBr:Sm^{++} is 0.7 cm^{-1}. The sideband is observed on the long wavelength side of this line, extending for 167 cm^{-1} in the case of KBr:Sm^{++} and for 215 cm^{-1} in the case of KCl:Sm^{++}. Beyond these frequencies there is a very low intensity continuum in the two-phonon region. The sharpest features of these sidebands can be measured to within 0.2 cm^{-1}.

The curves are direct recorder traces; and so no cor-

Figure 2. The sideband on the long-wavelength side of the 6890 Å transition of Sm^{++} in KBr at 7°K. The curve is a direct recorder trace. To obtain the luminescence in units of relative number of photons/unit wavelength, the curve must be divided by the photomultiplier response of figure 1.

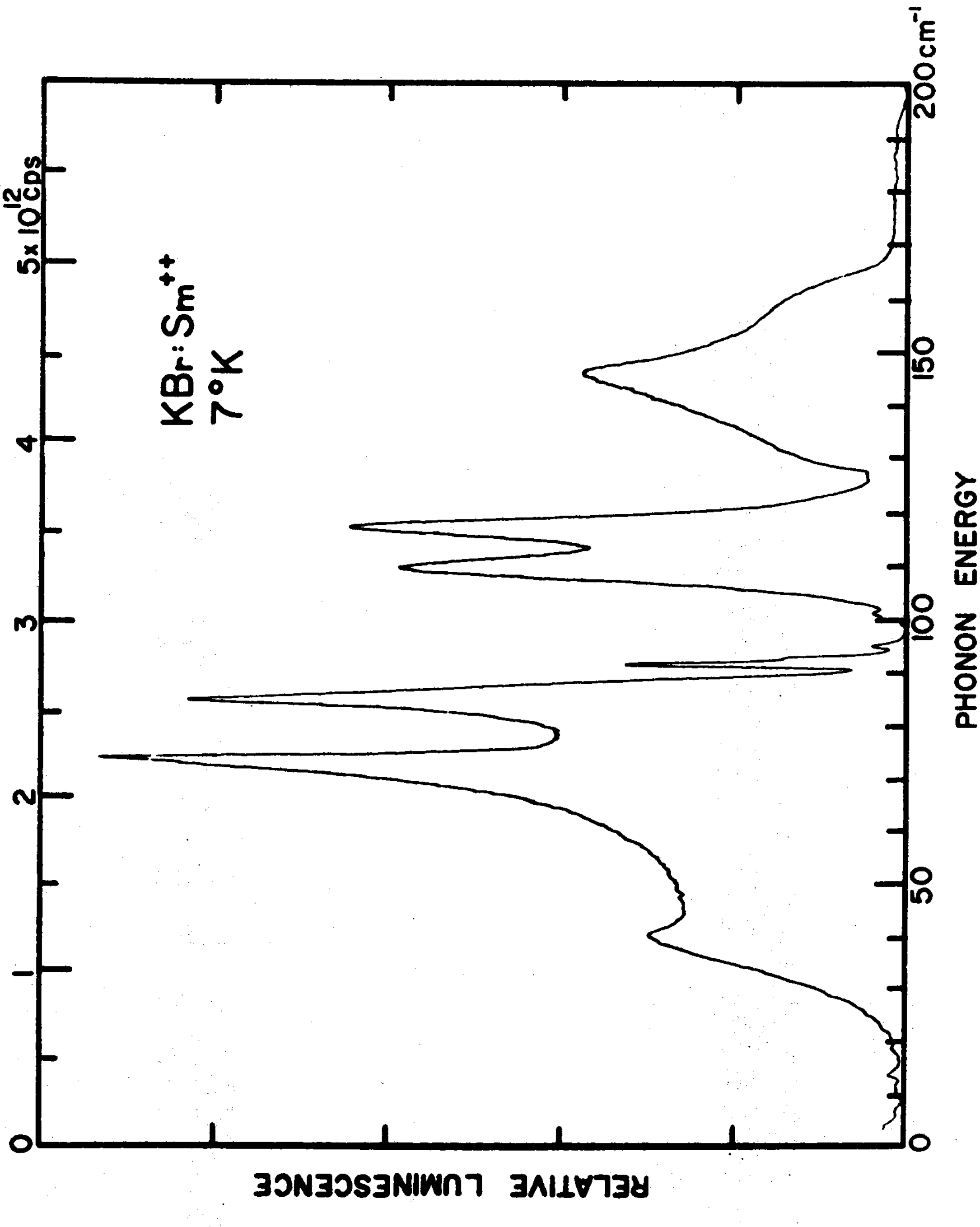
KBr : Sm++
7°K
RELATIVE LUMINESCENCE
PHONON ENERGY
0
1
2
3
4
5x10¹² cps
0
50
100
150
200 cm⁻¹

Figure 3. The sideband on the long-wavelength side of the 6892 Å transition of Sm^{++} in KCl. The peaks below 15 cm^{-1} vary from sample to sample, but the sideband does not. The curve is a direct recorder trace taken at 7°K. The ordinate scale is the same as figure 2 apart from a constant factor.

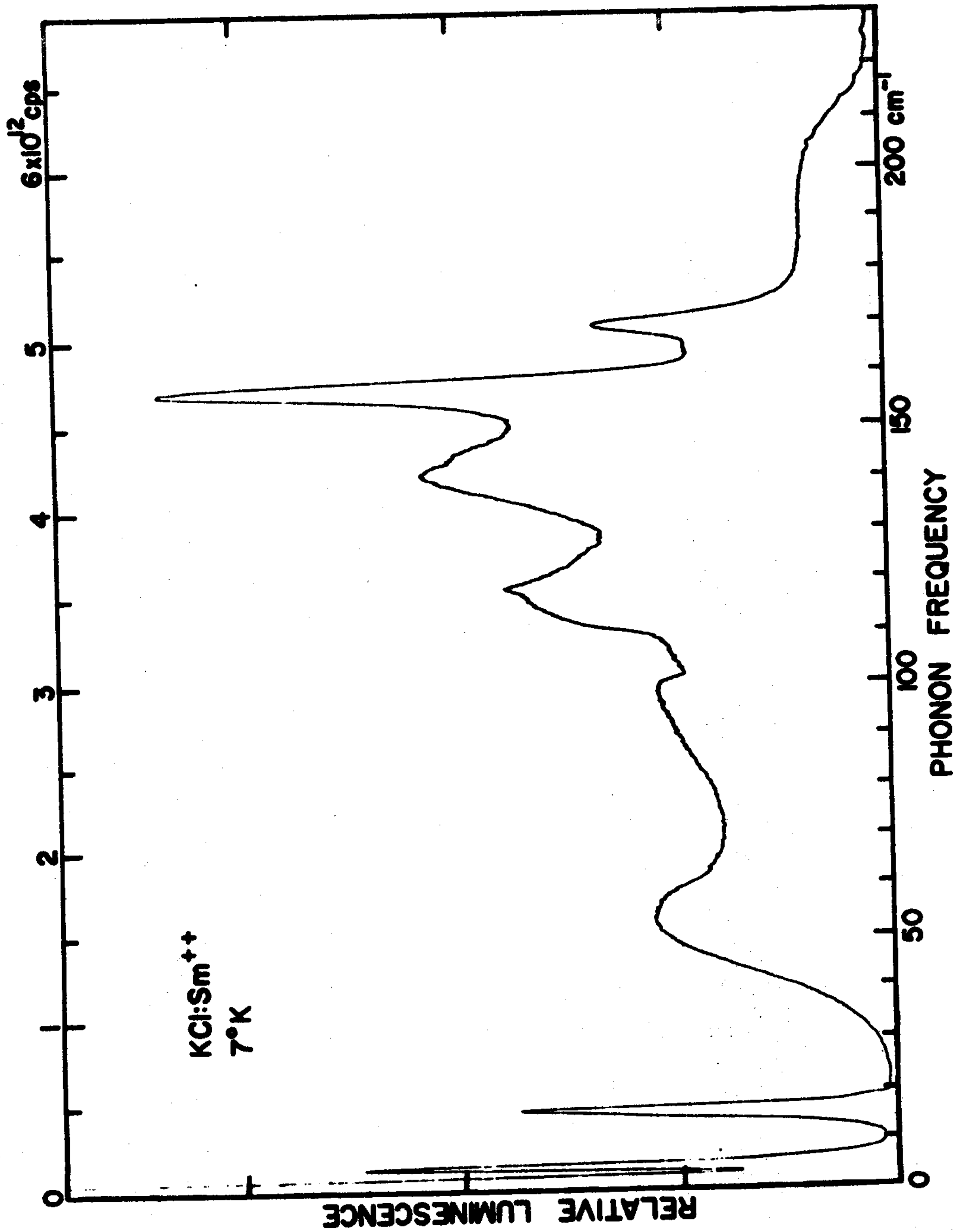
KCl:Sm⁺⁺
7°K
RELATIVE LUMINESCENCE
PHONON FREQUENCY
0
1
2
3
4
5
6x10¹² cps
0
50
100
150
200 cm⁻¹

rection has been made for photomultiplier sensitivity. As can be seen from the curves presented in section A for the response of the system, this correction amounts to about 25% across the one-phonon spectrum, and the higher frequencies should be enhanced by this factor over the lower ones. However since it is the structure and position of the various sharp features that are of primary interest here, this correction has not been made in the experimental curves.

The KBr:Sm^{++} curve is particularly striking; the spectrum is broken into two branches separated by a gap in frequency. In the acoustic branch, the spectrum rises to a distinctive "hook" at 40.5 cm^{-1}. This feature will be referred to as peak A. Beyond this, the acoustic spectrum has two sharp peaks at 74.7 cm^{-1} (B) and 85.7 cm^{-1} (C). These peaks are extremely sharp and are asymmetric. Above the gap, in the optic branch, there are two more peaks at 111 cm^{-1} (D) and 119 cm^{-1} (E). These peaks are somewhat more rounded in appearance than the two sharp peaks in the acoustic branch. Beyond this, a minimum is observed at 128 cm^{-1} followed by a smoothly rounded peak at 147 cm^{-1} (F). The 167 cm^{-1} range of frequencies observed for phonons in pure KBr by neutron measurements corresponds closely with that observed here, as does the gap from 95 to 100 cm^{-1}.

The peak at 93 cm^{-1} at the beginning of the gap in the KBr:Sm^{++} curves is always present, with a "shoulder" on the falling side. The possibility that this mode was due to chlorine as an impurity was investigated, since KBr:Cl$^-$ crystals exhibit a local mode at 95 cm^{-1} (Klein 1968). Sideband spectra were compared for three samples: KBr:SmBr$_3$, KBr:SmCl$_3$ (0.5 at.% Cl$^-$), and KBr:SmCl$_3$+KCl (5 at.% Cl$^-$). No change in the intensity or sharpness of the peak was observed.

An attempt was also made to ascertain whether or not this peak was a local mode due to Sm^{++}, with the peak and shoulder caused by the spread in naturally occurring isotopes. A crystal was prepared doped with isotopically enriched Sm^{154}Cl$_3$ supplied by Oak Ridge National Laboratories; this sample was expected to exhibit a decreased intensity of the "shoulder" with respect to the main peak if the mode was due to samarium. No such decrease was observed.

For KCl:Sm^{++} the sideband appears somewhat different; no gap is observed. Some of the features however are similar to those observed in the KBr:Sm^{++} sideband. A smoothly rounded peak at 53 cm^{-1} (A) is observed, followed by two sharp and distinctive features: a "step" at 100 cm^{-1} (B) and a strikingly shaped peak with a very sharp angle at 118.4 cm^{-1} (C). A double peak is observed at about 140 cm^{-1} (D,E), a sharp strong peak at 155 cm^{-1} (F) and a somewhat less sharp peak at 168 cm^{-1} (G). The spectrum ends abruptly at 215 cm^{-1} with only a very low intensity continuum beyond this point.

Several less obvious features in these sidebands are also to be noted. These features are completely reproducible, but do not show up very clearly on all traces because of lamp intensity fluctuations. The recorder trace in figure 4 shows a high resolution scan of the KBr:Sm^{++} sideband in the region between about 68 cm^{-1} and 90 cm^{-1}. There is a slight but abrupt change of slope 1.5 cm^{-1} below peak B, and a similar change of slope 3,9 cm^{-1} above peak C. These two pairs of features immediately call to mind the usual sketches of the contribution to the density of states of a pair of saddle point Van Hove singularities. In addition, there is a weak slope change 6.4 cm^{-1} below peak B and again 2.7 cm^{-1} below peak C. Their positions are indicated by arrows. Some of these features appear to be identifiable with features predicted by the shell model; these are also indicated in figure 5 by arrows, on a sketch of the KBr density of states.

The KCl:Sm^{++} spectrum exhibits several discontinuities in slope also, as shown in figure 6. Their positions are indicated by arrows. The discontinuity 1.9 cm^{-1} below the peak at 118.4 cm^{-1} and the peak itself are again reminiscent of a pair of saddle points, and the step B with discontinuities at 100 cm^{-1} and 101.5 cm^{-1} is also a striking feature. There is also a discontinuity at 61.2 cm^{-1}, after the rounded

Figure 4. Detail of the KBr:Sm^{++} sideband in the region from about 68 cm^{-1} to 90 cm^{-1}. The curve is a recorder trace taken at 7°K. Peaks B and C are labelled; four other singularities are indicated by arrows or by dashed continuations of the slopes. There is a discontinuity of slope 1.5 cm^{-1} below peak B, and one 3.9 cm^{-1} above peak C. There are also very weak reproducible features 6.4 cm^{-1} below peak B and 2.7 cm^{-1} below peak C. The frequencies of these four features are 68.3 cm^{-1}, 73.2 cm^{-1}, 83.0 cm^{-1} and 89.6 cm^{-1}.

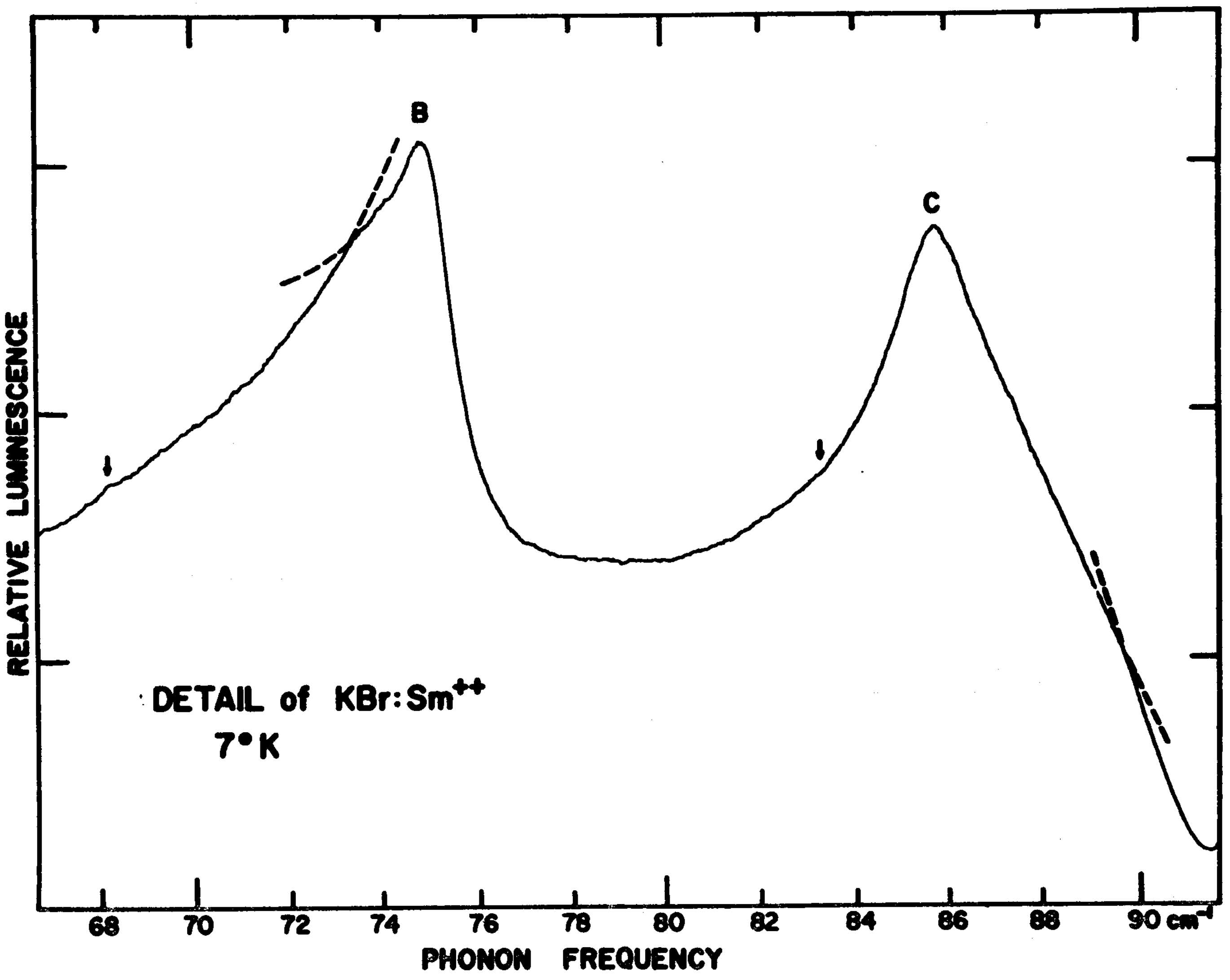
B
C
DETAIL of KBr:Sm^{++}
7° K
RELATIVE LUMINESCENCE
68
70
72
74
76
78
80
82
84
86
88
90 cm^{-1}
PHONON FREQUENCY

Figure 5. The total density of states for KBr, after Cowley and Cowley (1966). The positions of five of the singularities in figure 4 are indicated by the solid arrows. The open arrows indicate their positions shifted so that the strong peaks B and C correspond to their predicted positions. The observed discontinuities correspond closely to the predicted discontinuities, measured with respect to the strong peaks.

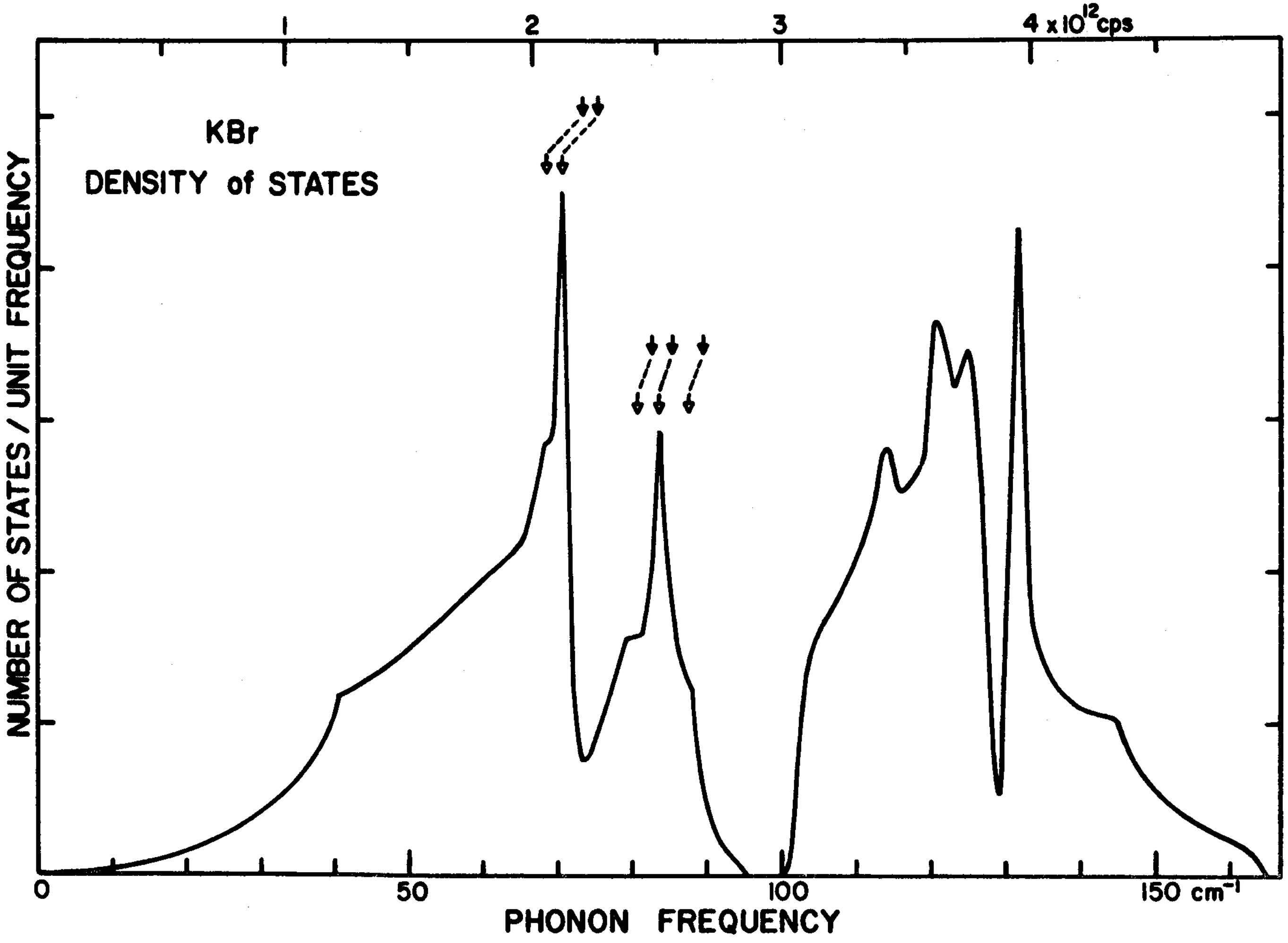
KBr
DENSITY of STATES
NUMBER OF STATES / UNIT FREQUENCY
PHONON FREQUENCY
0
50
100
150 cm⁻¹
1
2
3
4 x 10¹² cps

Figure 6. Detail of the KCl:Sm^{++} sideband in the region from about 70 cm^{-1} to 125 cm^{-1}. The curve is a recorder trace taken at 7°K. The peaks B and C are labelled. The positions of several discontinuities of slope are indicated by arrows. They occur at 101.5 cm^{-1}, 107.2 cm^{-1}, 108.4 cm^{-1}, and 116.5 cm^{-1}.

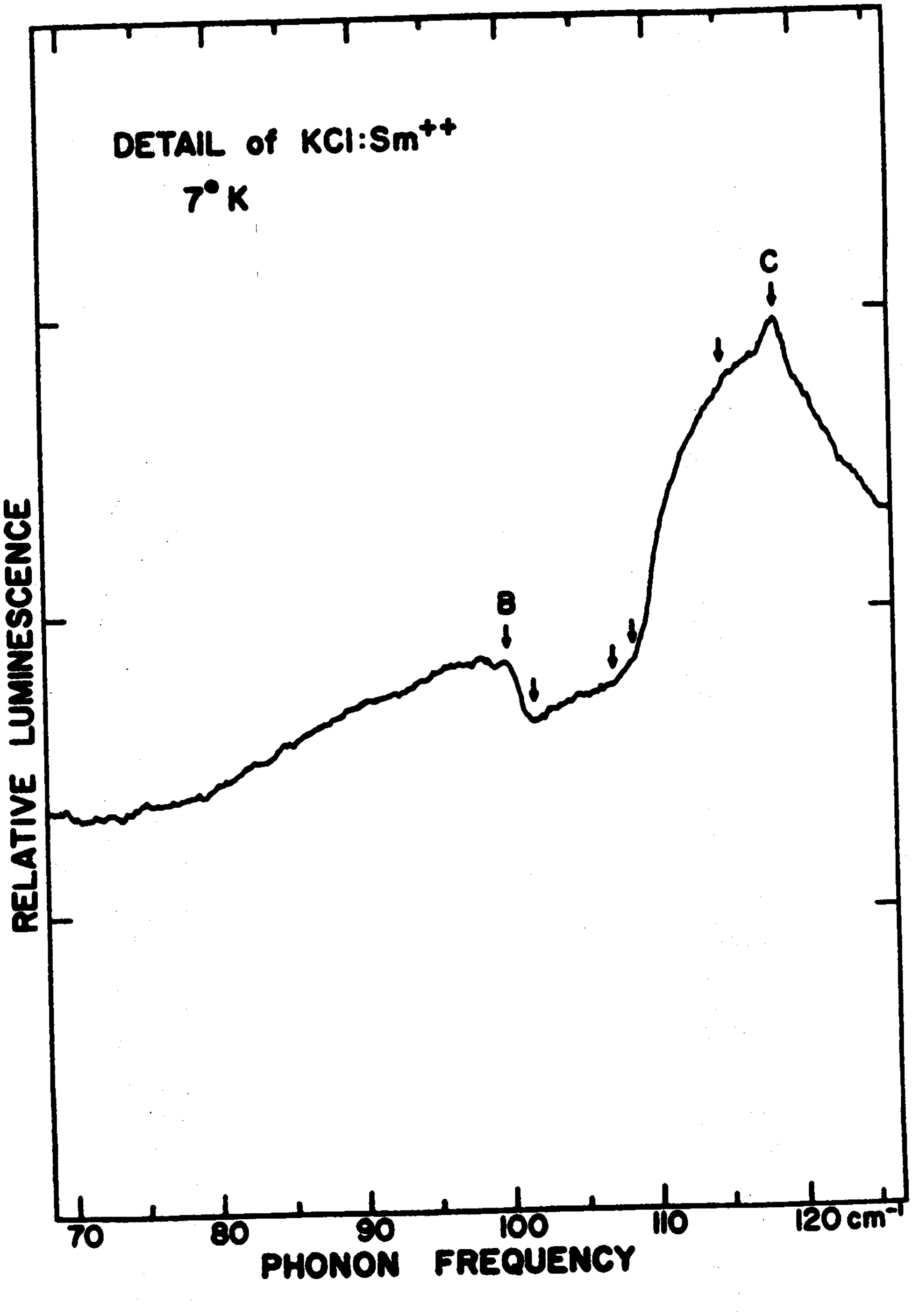
DETAIL of KCl:Sm++
7° K
B
C
RELATIVE LUMINESCENCE
70
80
90
100
110
120 cm⁻¹
PHONON FREQUENCY

peak at 53 cm^{-1}; this is clearly visible in figure 3. The KCl density of states is less well known than that for KBr, and it is hard to correlate these features with predicted singularities.

These high resolution measurements show that several of the sideband features have shapes characteristic of the phonon density of states which can be assigned to Van Hove singularities.

Vibrational modes are also observed accompanying the $^5D_0 \rightarrow {}^7F_1$ lines, but because of the complication of the three intense lines observed in this region, analysis and identification of vibrational frequencies is difficult.

In the case of these Sm^{++} doped samples, no difference between the sidebands of quenched and unquenched crystals was observed, although the zero-phonon line in unquenched samples showed several weak satellites within 15 cm^{-1} of itself.

Recorder traces are also presented of the one-phonon regions of the sideband spectra of $KBr:Eu^{++}$ and $KCl:Eu^{++}$ at 7°K (figures 7 and 8 respectively). Here, the zero-phonon lines fall at approximately 4107 Å for KBr and 4105 Å for KCl. These spectra are strikingly different in overall appearance from those of the samarium doped samples. Here many-phonon spectra are observed, extending for over 1200 cm^{-1} for both $KBr:Eu^{++}$ and $KCl:Eu^{++}$. The strongest features, corresponding

Figure 7. The one-phonon region of the sideband on the long-wavelength side of the 4107 Å transition of Eu^{++} in KBr at 7°K. The curve is a direct recorder trace. The labelled arrows indicate the peak positions observed in $KBr:Sm^{++}$.

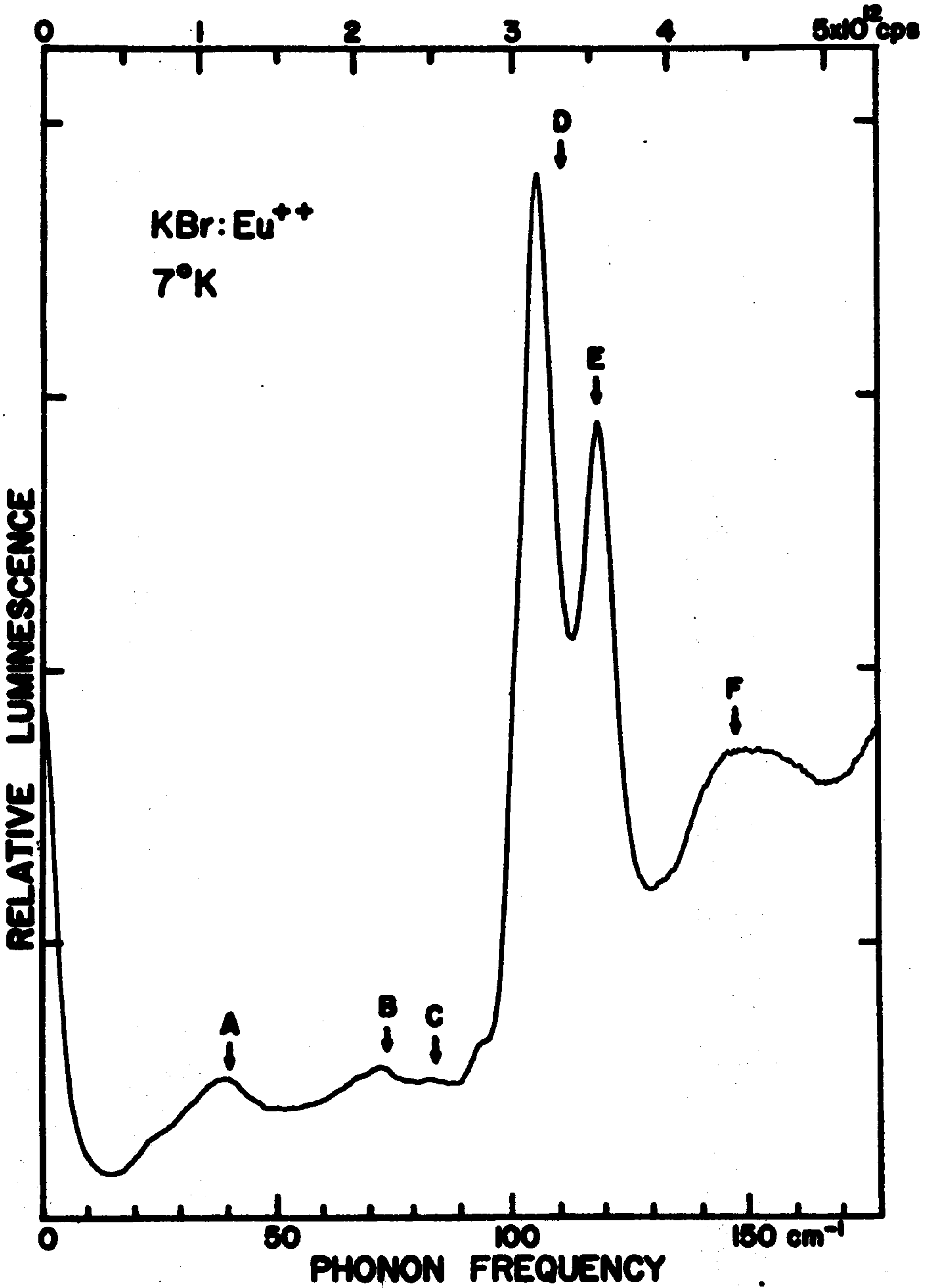
0
1
2
3
4
5x10^{12} cps
KBr:Eu^{++}
7°K
A
B
C
D
E
F
RELATIVE LUMINESCENCE
0
50
100
150 cm^{-1}
PHONON FREQUENCY

Figure 8. The one-phonon region of the sideband on the long-wavelength side of the 4105 Å transition of Eu^{++} in KCl at 7°K. The curve is a recorder trace. The labelled arrows indicate the peak positions observed in $KCl:Sm^{++}$.

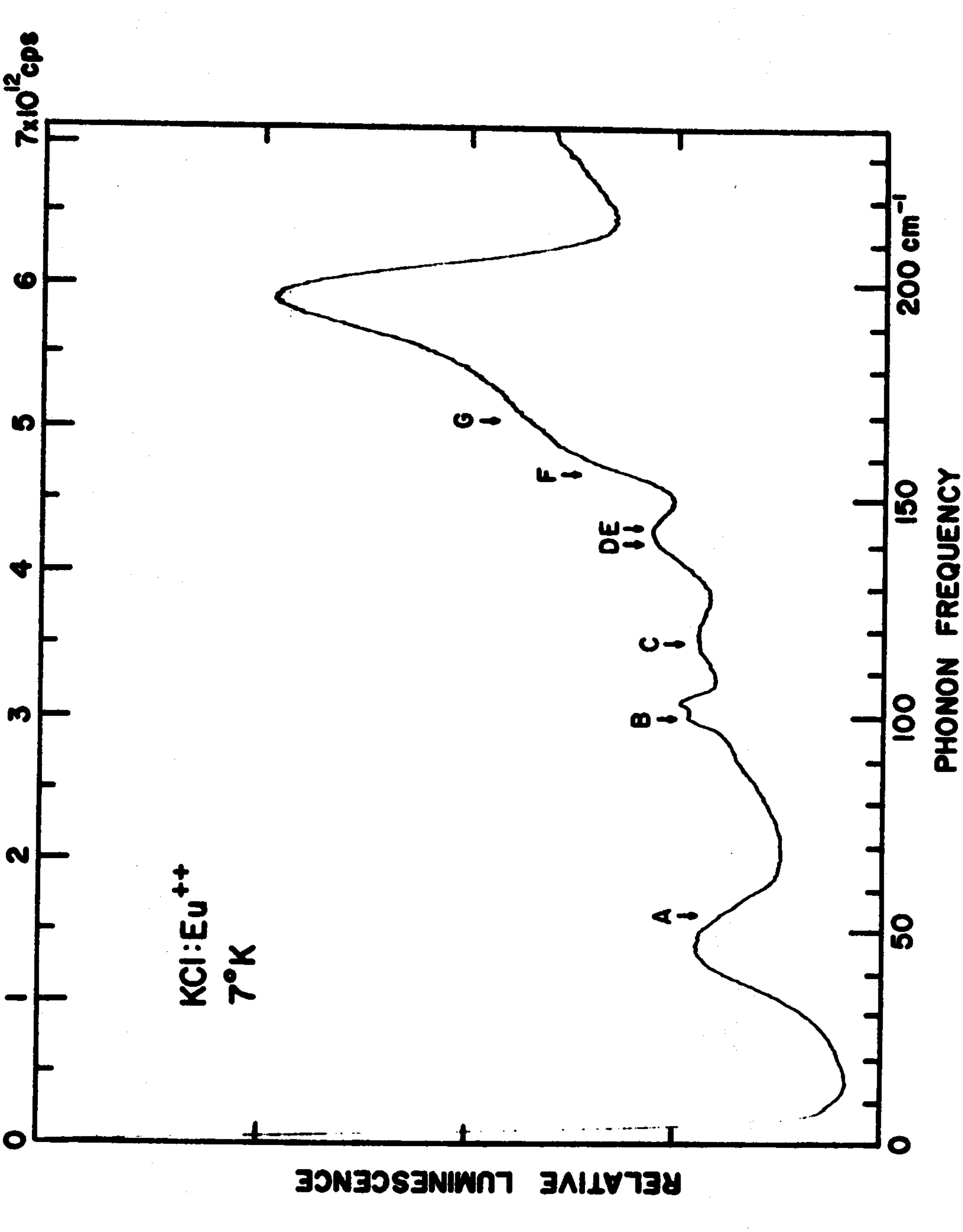
KCl:Eu++
7°K
RELATIVE LUMINESCENCE
PHONON FREQUENCY
0
1
2
3
4
5
6
7x10^12 cps
0
50
100
150
200 cm^-1
A
B
C
DE
F
G

to vibrational frequencies of 106 cm^{-1} and 119 cm^{-1} for KBr:Eu^{++} and 197 cm^{-1} for KCl:Eu^{++}, can be detected up to the five-phonon region for KBr and the four-phonon region for KCl.

In the one-phonon region in particular, both sidebands exhibit other features with much lower intensity than these sharp features. These show some similarities to the spectra of samarium-doped crystals, in peak position and shape. The arrows in figures 7 and 8 indicate the peak position observed in the samarium spectra.

Note in particular that the pair of peaks D and E in the optical branch of the KBr:Sm^{++} spectrum, while similar in appearance to the very sharp strong peaks in the KBr:Eu^{++} spectrum, do not agree in separation with them; and that the peaks F and G in the KCl:Sm^{++} spectrum do not appear at all in the KCl:Eu^{++} spectrum, which has instead a broad peak with maximum intensity at about 197 cm^{-1}.

Thus, the major differences in peak position between the crystals with the two dopants occurs for the strongest features of the spectra of the europium-doped samples.

The peak at 102 cm^{-1} in the KCl:Eu^{++} sideband is strongly concentration dependent, and thus appears to be due to pairs of europium ions. It is present in both quenched and unquenched crystals. Aside from this peak, the KCl:Eu^{++} spectrum for quenched crystals is somewhat simpler than that for unquenched crystals, as is the spectrum for $KBr:Eu^{++}$; several very weak peaks are seen in the spectra of unquenched crystals that are not seen in the quenched crystals.

CHAPTER 3

NOTATION AND BASIC FORMALISM

The system consists of a divalent ion present as a substitutional impurity in a cubic ionic lattice. The electronic levels of the rare-earth ion are perturbed by the presence of phonons in the lattice; at the same time, however, the motions of the lattice ions are perturbed by the foreign ion which replaces one of the potassium ions of the lattice.

It will be convenient to begin by defining the unperturbed systems and to review the unperturbed and perturbed lattice dynamics problems.

A. Zero order wave functions of the system

The total unperturbed wavefunctions of the system will be written $\Psi_n^\eta(\underline{r},\underline{R})$. Here $\underline{r}$ and $\underline{R}$ represent the time-dependent positions of the rare-earth ion electrons and the lattice ions respectively; n labels the electronic states and η the vibronic states of the lattice. It is assumed that the adiabatic approximation can be made so that Ψ can be separated into an electronic part ϕ and a lattice part χ:

$$\Psi_n^\eta(\underline{r},\underline{R}) = \phi_n(\underline{r},\underline{R})\chi_n^\eta(\underline{R}); \qquad (1)$$

and, further, that

$$\phi_n(\underline{r},\underline{R}) \cong \phi_n(\underline{r},\underline{R}_o), \qquad (2)$$

where $\underline{R}_o$ represents the equilibrium positions of the lattice ions. This second approximation is good for wave functions strongly localized in space about the impurity ion; it is probably generally good for the wave functions of a rare-earth ion in an alkali halide such as KBr or KCl since the ionic radius of divalent samarium, for example, is considerably smaller than that of potassium; in particular, it is a good approximation for the wave functions of the $4f^6$ (inner shell) configuration.

The wave functions ϕ are taken to satisfy the Schrödinger equation:

$$\{H_{el.}(\underline{r}) + H_{c.f.}(\underline{r},\underline{R})\}\phi_n(\underline{r},\underline{R}_o)=\varepsilon_n\ \phi_n(\underline{r},\underline{R}_o); \qquad (3)$$

here, $H_{el.}(\underline{r})$ is the Hamiltonian describing the free divalent samarium ion; $H_{c.f.}(\underline{r},\underline{R}_o)$ the perturbation resulting from the cubic crystal field; and ε_n the energy of the state ϕ_n. The wave functions ϕ transform as the representations of the cubic group.

B. Unperturbed lattice

The solutions of the unperturbed lattice problem - for the perfect lattice with no rare-earth impurity present - are fairly well established for alkali halide lattices; these are given by shell model calculations (Cowley et al. 1963) based on neutron diffraction measurements of the phonon frequencies. These solutions consist of a set of eigenvectors $\xi(\kappa \underline{q} j)$ and eigenfrequencies $\omega_{\underline{q}j}$, for the 6 branches numbered by j and a set of $\underline{q}$'s in the Brillouin zone. These eigenvectors and eigenvalues are the solutions of the equation

$$M_\kappa \ddot{u}_{L\kappa\alpha}(t) = \sum_{L'\kappa'\beta} \Phi_{\alpha\beta}\,(LL';\kappa\kappa')\,u_{L'\kappa'\beta}(t). \qquad (4)$$

Here $u_{L\kappa\alpha}(t)$ is the time-dependent displacement in the direction α, for the ion of type κ and mass M_κ in the unit cell L; κ takes on two values: $\kappa=1$ for K^+ and $\kappa=2$ for the halide ion.

The quantity $\Phi_{\alpha\beta}$ is defined:

$$\Phi_{\alpha\beta}(LL';\kappa\kappa') = \left[\frac{\partial^2}{\partial u_{L\kappa\alpha}\,\partial u_{L'\kappa'\beta}}\,\Phi(\underline{R})\right]_{\underline{R}_o} ; \qquad (5)$$

$\Phi(\underline{R})$ is the total potential of the crystal, composed of a repulsive part Φ^R and a Coulomb part Φ^C; the subscript $\underline{R}_o$ means that the derivative is to be evaluated at the equilibrium positions of the ions.

The time dependence of equation (4) is removed by making the substitution

$$u_{L\kappa\alpha}(t) = \frac{U_{L\kappa\alpha}}{\sqrt{M_\kappa}}\exp(-i\omega t) \qquad (6)$$

Equation (4) then becomes

$$\sum_{L'\kappa'\beta} \overset{\circ}{L}_{L\kappa\alpha,L'\kappa'\beta}\, U_{L'\kappa'\beta} = 0 \qquad (7)$$

where

$$\overset{\circ}{L}_{L\kappa\alpha,L'\kappa'\beta} = \frac{\Phi_{\alpha\beta}(LL';\kappa\kappa')}{\sqrt{M_\kappa M_{\kappa'}}} - \omega^2 \delta_{LL'}\delta_{\kappa\kappa'}\delta_{\alpha\beta}\,. \qquad (8)$$

Equation (7) can be diagonalized by a unitary transformation using the matrix $\underline{\underline{D}}$ where

$$D_{L\kappa\alpha,\underline{q}j} = \frac{1}{\sqrt{N}}\,\xi_\alpha(\kappa\underline{q}j)\,\exp(i\underline{q}\cdot\underline{R}_{L\kappa})\,. \qquad (9a)$$

The eigenvectors $\underline{\xi}(\kappa\underline{q}j)$ are real for this lattice, and the elements of $\underline{\underline{D}}^{-1}$ are

$$D_{\underline{q}j,L\kappa\alpha} = \frac{1}{\sqrt{N}}\,\xi_\alpha(\kappa\underline{q}j)\,\exp(-i\underline{q}\cdot\underline{R}_{L\kappa}) \qquad (9b)$$

The vector $\underline{R}_{L\kappa}$ gives the equilibrium position of the ion labelled by (L,κ); N is the number of ions in the lattice.

Then, in the $\{\underline{q}j\}$ space, $\underline{\underline{L}}^\circ$ is a diagonal matrix with elements

$$\overset{\circ}{L}_{\substack{\underline{q}\,j\\ \underline{q}'j'}} = (\omega^2_{\underline{q}j} - \omega^2)\,\delta_{\underline{q}\underline{q}'}\delta_{jj'}\;; \qquad (10)$$

and the set of equations given by (7) becomes a set

$$(\omega^2_{\underline{q}j} - \omega^2)\; Q_{\underline{q}j} = 0 \qquad (11)$$

for each mode $(\underline{q}j)$. The set $\{Q_{\underline{q}j}\}$ are the normal mode coordinates.

Since

$$\sum_{L\kappa\alpha} D_{\underline{q}j,L\kappa\alpha}\, U_{L\kappa\alpha} = Q_{\underline{q}j}\ , \tag{12}$$

the displacement $\mu_{L\kappa\alpha}(t)$ can be written:

$$\mu_{L\kappa\alpha}(t) = \frac{e^{-i\omega t}}{\sqrt{M_\kappa}} \sum_{\underline{q}j} D_{L\kappa\alpha,\underline{q}j}\, Q_{\underline{q}j}$$

$$= \frac{1}{\sqrt{NM_\kappa}} \sum_{\underline{q}j} \xi_\alpha(\kappa\underline{q}j)\, e^{i(\underline{q}.\underline{R}_{L\kappa}-\omega t)}\, Q_{\underline{q}j}\ . \tag{13}$$

The wave functions $\chi(R)$ satisfy the set of Schrödinger equations:

$$\frac{1}{2}\{\omega^2 Q^2_{\underline{q}j} - \frac{\hbar^2\partial^2}{\partial Q^2_{\underline{q}j}}\}\ \chi^\eta(\underline{R}) = \hbar\omega_{\underline{q}j}(\eta + \frac{1}{2})\ \chi^\eta(\underline{R}) \tag{14}$$

where η gives the number of phonons of type $(\underline{q}j)$ in the state. These χ's are harmonic oscillator wave functions and have the following properties:

$$<\chi^\eta(\underline{R})|\chi^\eta(\underline{R})> = \delta_{\eta\eta'},$$

$$<\chi^1(\underline{R})|Q_{\underline{q}j}|\chi^0(\underline{R})> = \sqrt{\frac{\hbar}{2\omega_{\underline{q}j}}}\ ; \tag{15}$$

here, $\chi^0(\underline{R})$ represents a lattice state with no phonons present; $\chi^1(\underline{R})$ is the wave function of the state with one phonon of the type $(\underline{q}j)$ excited. These matrix elements will be the only ones needed for this problem.

The assumption that the phonon wave functions do not depend on the electronic quantum number n is central to the mechanism that will be considered here. The assumption that χ_n^η depends on n leads to a different frequency dependence for the sideband from that observed, and to a stronger two-phonon sideband than is observed; this will be shown in Appendix C.

C. Perturbed lattice

It will be convenient to define the Green's function of the unperturbed lattice, $\underline{\underline{G}}^\circ$:

$$\underline{\underline{L}}^\circ \underline{\underline{G}}^\circ = \underline{\underline{I}}. \tag{16}$$

In the $\{\underline{q}j\}$ space, $\underline{\underline{G}}^\circ$ can be directly written:

$$G^\circ_{\underline{q}j}(\omega) = \frac{1}{\omega^2_{\underline{q}j} - \omega^2} \quad ; \tag{17}$$

and thus, in the real $(L\kappa\alpha)$ space,

$$G^\circ_{L\kappa\alpha,L'\kappa'\beta}(\omega) = \sum_{\underline{q}j} D_{L\kappa\alpha,\underline{q}j}\, G^\circ_{\underline{q}j}(\omega)\, D_{\underline{q}j,L'\kappa'\beta}$$

$$= \frac{1}{N} \sum_{\underline{q}j} \frac{\xi_\alpha(\kappa\underline{q}j)\xi_\beta(\kappa'\underline{q}j)}{\omega^2_{\underline{q}j} - \omega^2} \exp(i\underline{q}\cdot(\underline{R}_{L\kappa} - \underline{R}_{L'\kappa'})) \ . \tag{18}$$

Note that

$$\mathrm{Im}\ G^\circ_{\underline{q}j}(\omega + i0^+) = \frac{\pi}{2\omega_{\underline{q}j}}\, \delta(\omega_{\underline{q}j} - \omega) \tag{19}$$

and that the exponential in equation (18) gives a completely real contribution, so that

$$\mathrm{Im}\ G^{\circ}_{L\kappa\alpha,L'\kappa'\beta}\ (\omega+i0^{+}) = \sum_{\underline{q}j} D_{L\kappa\alpha,\underline{q}j}\{\mathrm{Im}\ G^{\circ}_{\underline{q}j}(\omega+i0^{+})\} \times D_{\underline{q}j,L'\kappa'\beta} \qquad (20)$$

The perturbed lattice satisfies an equation of motion similar to equation 7, with $\underline{\underline{L}}^{\circ}(\omega)$ replaced by $\underline{\underline{L}}(\omega)$ and $\underline{U}$ giving the displacement of the ions in perturbed lattice. The matrix $\underline{\underline{L}}(\omega)$ is related to $\underline{\underline{L}}^{\circ}(\omega)$ by

$$\underline{\underline{L}}(\omega) = \underline{\underline{L}}^{\circ}(\omega) + \underline{\underline{\Gamma}}(\omega)\ , \qquad (21)$$

where $\underline{\underline{\Gamma}}(\omega)$ is a matrix giving the changes from the perfect lattice.

A perturbed Green's function G can then be defined, by

$$\underline{\underline{G}}\ \underline{\underline{L}} = \underline{\underline{I}}, \qquad (22)$$

and $\underline{\underline{G}}$ can be solved for in terms of $\underline{\underline{G}}^{\circ}$ and Γ; for

$$\underline{\underline{G}}(\underline{\underline{L}}^{\circ} + \Gamma) = \underline{\underline{I}}$$

so

$$\underline{\underline{G}} + \underline{\underline{G}}\underline{\underline{\Gamma}}\underline{\underline{G}}^{\circ} = \underline{\underline{G}}^{\circ}$$

or

$$\underline{\underline{G}} = \underline{\underline{G}}^{\circ}[\underline{\underline{I}} + \underline{\underline{\Gamma}}\underline{\underline{G}}^{\circ}]^{-1}\ . \qquad (23)$$

Equation (23) can also be written, defining

$$\underline{\underline{T}} = \underline{\underline{\Gamma}}[\underline{\underline{I}} + \underline{\underline{G}}^{\circ}\underline{\underline{\Gamma}}]^{-1} \qquad (24)$$

as

$$\underline{\underline{G}} = \underline{\underline{G}}^{\circ} - \underline{\underline{G}}^{\circ}\underline{\underline{T}}\underline{\underline{G}}^{\circ}\ ; \qquad (25)$$

$\underline{\underline{T}}$ is the "scattering matrix" as defined by Klein (1963).

In applications where all elements of $\underline{\underline{G}}$ are needed, equation (25) is a more useful form than equation (23).

Since $\underline{\underline{\Gamma}}$ usually has only a few non-zero elements in a small subspace about the impurity ion, $[\underline{\underline{I}} + \underline{\underline{G}}^{\circ}\underline{\underline{\Gamma}}]$ can be inverted, making use of theorems on the partition of matrices. Then $\underline{\underline{T}}$ also has non-zero elements only in the small subspace.

D. Simplifications as a result of symmetry

The most reasonable first approximation is the assumption of cubic symmetry for the unperturbed electronic problem. Fong and Wong (1967) found many inequivalent sites for the charge compensating defect, including some at large distances from the rare-earth ion, so this assumption is not unreasonable, and it would be unrealistic to base one's calculations on the the vacancy being at $(\frac{a}{2},\frac{a}{2},0)$ as did Bron and co-workers. The assumption of cubic symmetry also has the aspect of simplifying greatly the solution of the problem; for the summations over all ions that are implied by the long-range Coulomb nature of the coupling between the lattice ions and the rare-earth ion can be made straightforwardly, as will be seen in the next chapter; while the perturbed lattice problem is greatly simplified by the assumption that $\underline{\underline{\Gamma}}$ does not lower the symmetry from cubic.

Note that the assumption of cubic symmetry enters in two places: for the symmetry of the zero-order electronic wave functions, and for the perturbation of the lattice. While it might be reasonable to use non-cubic wave functions and a cubic $\underline{\underline{\Gamma}}$, the use of cubic wave functions and a non-cubic $\underline{\underline{\Gamma}}$ would not be reasonable, since $\underline{\underline{\Gamma}}$ represents changes very close to the impurity. Problems arising from the assumption of non-cubic wave functions will be mentioned further in Chapter 5.

If $\underline{\underline{\Gamma}}$ has cubic symmetry, the lattice problem can be treated most easily by transforming from the real $(L\kappa\alpha)$ space to a space spanned by motions corresponding to the representations of the cubic group; for in this space both $\underline{\underline{G}}^{\circ}$ and $\underline{\underline{\Gamma}}$ become block diagonal since the rows of the cubic representations do not couple. In this space the matrix $[\underline{\underline{I}} + \underline{\underline{G}}^{\circ}\underline{\underline{\Gamma}}]$ can be inverted easily since the various blocks do not affect each other. The transformations to this 'cubic' space are given in Appendix A.

CHAPTER 4

SIDEBAND OF THE $^5D_0 \rightarrow {}^7F_0$ TRANSITION OF SAMARIUM IN ALKALI HALIDES

A. Perturbation Hamiltonian and transition probability

The $^5D_0 \rightarrow {}^7F_0$ transition giving rise to the line observed in the low temperature luminescence of KBr and KCl crystals containing divalent samarium is between two levels of even parity. In a cubic environment, both levels have A_{1g} symmetry. The transition, therefore, is strictly forbidden. The presence of other defects or of phonons in the host crystal, however, lowers the site symmetry of the samarium ion and allows the transition by mixing the odd-parity states. It is assumed in this thesis that these defects and phonons are coupled to the rare-earth ion by the Coulomb field they cause at the samarium site. Positive ion vacancies, which are necessarily present in the monovalent crystal to compensate for the double charge of the rare-earth ion, will cause a static field at the Sm^{++} site and give rise to the zero-phonon line; while phonons in the ionic lattice cause a time dependent field and give rise to a sideband extending over the range of phonon frequencies.

The interaction Hamiltonian, H^I, has thus been assumed to be of the form

$$H^I = H_P + H_S + H_Q; \qquad (1)$$

here H_P represents the interaction of the Sm^{++} electrons with the photon field, H_S their interaction with charge-compensating vacancies, and H_Q their interaction with the phonons of the lattice. H_Q can be written

$$H_Q = \sum_{\underline{q}} H_{\underline{q}} \qquad (2)$$

since the phonons are independent of each other in the harmonic approximation.

The transition is forbidden in first order but is allowed in second order if the intermediate state is of the appropriate symmetry; one can write the transition probability per unit time, $W_{e\to g}$, directly, using second order time dependent perturbation theory (Schiff 1955)

$$W_{e\to g} = \frac{2\pi}{\hbar} \sum_{\substack{\text{final} \\ \text{states}}} \left| \sum_i \frac{<\Psi_g|H^I|\Psi_i><\Psi_i|H^I|\Psi_e>}{E_i - E_e} \right|^2$$

$$\times\ \delta(E_g - E_e)\ . \qquad (3)$$

Here Ψ_e, Ψ_i, and Ψ_g are the wave functions of the excited intermediate and ground states, respectively, and E_e, E_i, and E_g their energies. The Ψ's are of the form discussed in Chapter 3. The summation on i extends over all intermediate states.

The phonon sideband corresponds to the creation of a photon of energy $\hbar\omega_{\underline{p}}$ with a phonon of energy $\hbar\omega_{\underline{q}}$, where

$$\hbar\omega_{\underline{p}} + \hbar\omega_{\underline{q}} = \varepsilon_e - \varepsilon_g \tag{4}$$

to satisfy the δ-function in equation (3); ε_e and ε_g are the energies of the unperturbed electronic states as defined in Chapter 3.

Thus the expression for the sideband transition probability becomes

$$W_{e\to g} = \frac{2\pi}{\hbar} \sum_{\{\underline{p},\underline{q}\}} \left| \sum_i \left\{ \frac{\langle\chi^1\phi_g|H_p|\chi^1\phi_i\rangle\langle\chi^1\phi_i|H_q|\chi^0\phi_e\rangle}{\varepsilon_i + \hbar\omega_{\underline{q}} - \varepsilon_e} + \frac{\langle\chi^1\phi_g|H_q|\chi^0\phi_i\rangle\langle\chi^0\phi_i|H_p|\chi^0\phi_e\rangle}{\varepsilon_i + \hbar\omega_{\underline{p}} - \varepsilon_e} \right\} \right|^2$$

$$\times\ \delta(\varepsilon_g + \hbar\omega_{\underline{q}} + \hbar\omega_{\underline{p}} - \varepsilon_e) \tag{5}$$

where the set $\{\underline{p},\underline{q}\}$ are related by equation (4), and they define the possible final states since ϕ_g is non-degenerate.

The largest contribution to the sideband arises from electric dipole terms; for these, $H_p = e\underline{E}\cdot\underline{r}$ where $\underline{E}$ is the electric field of the photons. Thus, for a final state with photons polarized along the x direction, H_p transforms like $T_{1u}{}^x$. Then, writing the electronic part of the matrix elements that appear in equation (5) with the symmetry in r explicit one has:

$$\langle\phi_g(A_{1g})|H_p(T_{1u}{}^x)|\phi_i(\Gamma^i)\rangle\langle\phi_i(\Gamma^i)|H_q(\Gamma^j)|\phi_e(A_{1g})\rangle, \tag{6}$$

which is zero unless $\Gamma^i = \Gamma^j = T_{1u}{}^x$. Thus, the part of H_q which enters must have $T_{1u}{}^x$ symmetry in $\underline{r}$, as must the intermediate states ϕ_i.

Equation (5) can be simplified further by making the approximations

$$\varepsilon_i + \hbar\omega_{\underline{q}} - \varepsilon_e \cong \varepsilon_i - \varepsilon_e$$

and

$$\varepsilon_i + \hbar\omega_{\underline{p}} - \varepsilon_e = \varepsilon_i - \hbar\omega_{\underline{q}} - \varepsilon_g \cong \varepsilon_i - \varepsilon_g; \qquad (7)$$

for the energies of the necessary $T_{1u}{}^x$-symmetry levels are not near those of ϕ_g or ϕ_e, as they belong to the $4f^5 5d$ configuration. At worst, a level of $T_{1u}{}^x$ symmetry nearby would cause a smooth and monotonically varying ω-dependent factor, strengthening the low frequency contribution to the calculated sideband with respect to the high frequency contribution.

Assuming that the ions of the lattice may be treated as point charges for the purpose of finding their Coulomb field at the position of the samarium electrons, and that the electronic states of the Sm^{++} ion are so strongly localized that overlap with other ions may be neglected (justifiable as the transition is between inner-shell levels), the Hamiltonian H_Q may be written:

$$H_Q = \sum_{L\kappa \neq 01} \left\{ \frac{e^2 Z_\kappa}{|\underline{R}_{L\kappa} + \underline{u}_{L\kappa} - \underline{u}_{01} - \underline{r}|} - \frac{e^2 Z_\kappa}{|\underline{R}_{L\kappa} - \underline{r}|} \right\} \quad (8)$$

where Z_κ is the charge of the ion at $\underline{R}_{L\kappa}$. The equilibrium position of the samarium ion has been taken as the origin of the lattice ($\underline{R}_{01} = 0$), and $\underline{r}$ is the displacement of the samarium electrons from the nucleus at $\underline{u}_{01}$. The terms $\frac{e^2 Z_\kappa}{|\underline{R}_{L\kappa}-\underline{r}|}$ are subtracted as these were included in the crystal field Hamiltonian $H_{c.f.}$; the wave functions ϕ_n are assumed to have been solved for including these terms.

Equation (8) can now be expanded in a MacLaurin series in $\underline{r}$; the lowest order terms of $T_{1u}{}^{x}$ symmetry in $\underline{r}$ are

$$H_Q^1(T_{1u}{}^{x}) = \sum_{L\kappa\neq 01} e^2 Z_\kappa \left\{\frac{R_{L\kappa x} + u_{L\kappa x} - u_{01x}}{|\underline{R}_{L\kappa} + \underline{u}_{L\kappa} - \underline{u}_{01}|^3} - \frac{R_{L\kappa x}}{|\underline{R}_{L\kappa}|^3}\right\} r_x \quad (9)$$

This may be further expanded, since $|\underline{u}_{L\kappa} - \underline{u}_{01}| << |\underline{R}_{L\kappa}|$:

$$H_Q^1 = \sum_{L\kappa\neq 01} e^2 Z_\kappa \left\{\frac{(u_{L\kappa x}-u_{01x})}{|\underline{R}_{L\kappa}|^3} - \frac{3R_{L\kappa x}\underline{R}_{L\kappa}\cdot(\underline{u}_{L\kappa}-\underline{u}_{01})}{|\underline{R}_{L\kappa}|^5}\right\} r_x \quad (10)$$

to terms linear in $(\underline{u}_{L\kappa}-\underline{u}_{01})$. Note that

$$\sum_{L\kappa\neq 01} \left\{\frac{u_{01x}}{|\underline{R}_{L\kappa}|^3} - \frac{3R_{L\kappa x}(\underline{R}_{L\kappa}\cdot\underline{u}_{01})}{|\underline{R}_{L\kappa}|^5}\right\} = 0 \quad (11)$$

in cubic symmetry (Kittel 1956) and that

$$\sum_{L\kappa\neq 01} e^2 Z_\kappa \left\{\frac{u_{L\kappa x}}{|\underline{R}_{L\kappa}|^3} - \frac{3R_{L\kappa x}(\underline{R}_{L\kappa}\cdot\underline{u}_{L\kappa})}{|\underline{R}_{L\kappa}|^5}\right\}$$

$$= \sum_{L\kappa\neq 01} e^2 Z_\kappa \left\{\frac{\underline{R}_{L\kappa}^2\,\delta_{\alpha x} - 3R_{L\kappa x}R_{L\kappa\alpha}}{|\underline{R}_{L\kappa}|^5}\right\} u_{L\kappa\alpha}$$

$$= \sum_{L\kappa\neq 01} \left| \frac{\partial^2}{\partial u_{L\kappa\alpha}\,\partial u_{01x}} \left(\frac{e^2 Z_\kappa}{|\underline{R}_{L\kappa} + \underline{u}_{L\kappa} - \underline{u}_{01}|} \right) \right|_{\underline{R}_{L\kappa}} u_{L\kappa\alpha}$$

$$= \sum_{L\kappa\alpha} Z_\kappa\, \Phi^{C}_{x\alpha}(0L,1\kappa)\, u_{L\kappa\alpha} \quad . \qquad (12)$$

In the last line of equation (12) the restriction on the summation has been removed, using

$$\Phi^{C}_{\alpha\beta}(00,11) = -\sum_{L\kappa\neq 01} \Phi^{C}_{\alpha\beta}(0L;1\kappa) \equiv 0$$

for cubic symmetry.

H^1_Q can be written

$$H^1_Q = \frac{1}{\sqrt{N}} \sum_{\substack{\kappa\alpha\\ \underline{q}j}} \overset{1\kappa}{\underset{\underline{q}}{C(x\alpha)}}\; \frac{\xi_\alpha(\kappa\underline{q}j)}{\sqrt{M_\kappa}}\; Q_{\underline{q}j} \qquad (13)$$

using $u_{L\kappa\alpha}$ as given in Chapter 3. Here the factors $\overset{1\kappa}{\underset{\underline{q}}{C(x\alpha)}}$ are fourier transforms of $\Phi^{C}_{x\alpha}(0L;1\kappa)$:

$$\overset{1\kappa}{\underset{\underline{q}}{C(x\alpha)}} = \sum_{L} \Phi^{C}_{x\alpha}(0L;1\kappa)\, \exp(i\underline{q}\cdot\underline{R}_{L\kappa}) ; \qquad (14)$$

they have been evaluated by the Ewald method (Kellerman 1940). Equation (13) gives the Hamiltonian H_Q explicitly split into a sum on normal modes as in equation (2).

The transition probability of equation (5) can now be written, under the assumption that $\phi(\underline{r},\underline{R}) = \phi(\underline{r},\underline{R}_0)$, and using the expressions for the χ matrix elements. For x-polarized photons between $\omega_{\underline{p}}$ and $\omega_{\underline{p}}+\Delta\omega$, observed in solid angle $\Delta\Omega$, the transition rate is:

$$W_{e\to g} = \frac{\Delta\Omega\omega_o\,\Delta\omega}{2\pi\hbar c^3}\, e^2 \left|\sum_i \langle\phi_g|r_x|\phi_i\rangle\langle\phi_i|r_x|\phi_e\rangle \times \left\{\frac{\varepsilon_i - \varepsilon_g}{\varepsilon_i - \varepsilon_e} + \frac{\varepsilon_e - \varepsilon_i}{\varepsilon_i - \varepsilon_g}\right\}\right|^2 \frac{\hbar}{\pi}\, W(\omega) \qquad (15)$$

where the initial factor gives the density of final states in a standard way (Davydov 1966), with the approximation

$$\omega_{\underline{p}} = \frac{\varepsilon_e - \varepsilon_g}{\hbar} - \omega_{\underline{q}} \simeq \frac{\varepsilon_e - \varepsilon_g}{\hbar} = \omega_o. \qquad (16)$$

The factor $W(\omega)$ is given by

$$W(\omega) = \frac{\pi}{\hbar}\frac{1}{N}\sum_{\underline{q}j}\left\{\sum_{\kappa\alpha} Z_\kappa\, \overset{1\kappa}{\underset{\underline{q}}{C(x\alpha)}}\, \frac{\xi_\alpha(\kappa\underline{q}j)}{\sqrt{M_\kappa}}\sqrt{\frac{\hbar}{2\omega_{\underline{q}j}}}\right\}^2 \delta(\omega_{\underline{q}j}-\omega). \qquad (17)$$

Here, ω is defined by

$$\hbar\omega = \varepsilon_e - \varepsilon_g - \hbar\omega_{\underline{p}},$$

and is the phonon frequency measured with respect to the zero phonon line in the direction of decreasing energy. This expression was used by Timusk and Buchanan (1967) to calculate the sideband for KBr:Sm^{++}.

B. Formulation in terms of Green's functions

Equation (16) can be rewritten by identifying

$$\frac{\pi}{2\omega_{\underline{q}j}}\,\delta(\omega_{\underline{q}j}-\omega)$$

as the imaginary part of the Green's function in $\{\underline{q}j\}$ space, $\text{Im}\ G^\circ_{\underline{q}j}(\omega+i0^+)$. Then,

$$W(\omega) = \text{Im}\,\frac{1}{N}\sum_{\underline{q}j}\ \sum_{\substack{\kappa\ \alpha \\ \kappa'\beta}} \frac{Z_\kappa C\begin{pmatrix} 1\kappa \\ x\alpha \\ \underline{q} \end{pmatrix}}{\sqrt{M_\kappa}}\ \xi_\alpha(\kappa\underline{q}j)\ G^\circ_{\underline{q}j}(\omega+i0^+)$$

$$\times\ \frac{\xi_\beta(\kappa'\underline{q}j)\ C\begin{pmatrix} \kappa'1 \\ \alpha\ x \\ \underline{q} \end{pmatrix}\ Z_{\kappa'}}{\sqrt{M_{\kappa'}}}$$

$$= \text{Im}\sum_{\substack{L\ \kappa\ \alpha \\ L'\kappa'\beta}} Z_\kappa\ \frac{\Phi^C_{x\alpha}(0L;1\kappa)}{\sqrt{M_\kappa}}\ G^\circ_{L\kappa\alpha,L'\kappa'\beta}\ (\omega + i0^+)$$

$$\times\ \frac{\Phi^C_{\beta x}(L'0;\kappa'1)}{\sqrt{M_{\kappa'}}}\ Z_{\kappa'} \qquad (18)$$

since the factors $\underline{\xi}$, $\underline{\underline{C}}$, and $\underline{\underline{\Phi}}^C$ are all real numbers for this lattice.

Equation 18 is a convenient form for the treatment of the problem including the perturbation of the lattice by the samarium ion. For the perturbed problem, $\underline{\underline{G}}^\circ$ must be replaced by $\underline{\underline{G}}$, which describes the displacements of all ions and the frequencies of all modes for the lattice containing the defect. However, this is the only factor which changes; for the quantity $\Phi^C_{\alpha\beta}(0L;1\kappa)$ is dependent only on the symmetry of the lattice and on the equilibrium positions of all ions, which will be assumed to be unchanged; while $Z_\kappa/\sqrt{M_\kappa}$ is only changed for the origin term ($L = 0$, $\kappa = 1$), and this term does not contribute since $\Phi^{C}_{\alpha\beta}(00,11) \equiv 0$ for cubic symmetry.

Thus, for the perturbed lattice,

$$W(\omega) = \mathrm{Im} \sum_{\substack{L\,\kappa\,\alpha \\ L'\kappa'\beta}} Z_{\kappa} \frac{\Phi^{C}_{x\alpha}(0L;1\kappa)}{\sqrt{M_{\kappa}}} G_{L\kappa\alpha,L'\kappa'\beta}\,(\omega + i0^{+}) \times \frac{\Phi^{C}_{\beta x}(L'0;\kappa'1)}{\sqrt{M_{\kappa'}}} Z_{\kappa'} , \qquad (19)$$

with G given by

$$\underline{\underline{G}} = \underline{\underline{G}}^{\circ} - \underline{\underline{G}}^{\circ}\underline{\underline{T}}\,\underline{\underline{G}}^{\circ} .$$

C. Choice of $\underline{\Gamma}$

It is assumed that $\underline{\Gamma}$, the matrix of mass and force constant changes for the lattice due to the presence of the samarium ion, can be described by a small number of changes localized about the impurity site. Thus, it has been assumed that the effect of the double charge on the samarium ion can be neglected after a few neighbours; it is certainly true, at least, that its effect on distant ions is screened by the presence of charge compensating defects.

An attempt has been made to approximate the true situation by changes in a very localized region about the defect ion. The mass at the origin is changed from M_1 to M'; the force constants connecting this ion to its first neighbours and the force constants connecting the first neighbours to their nearest neighbours (the fourth neighbours of the impurity ion) are changed.

This model for $\underline{\underline{\Gamma}}$ is chosen because the increased Coulomb field due to the double charge of the samarium ion will tend to shift the equilibrium position of the nearest neighbours towards the samarium ion. The force constant, f, connecting the origin ion to its first neighbour is increased as a result of the smaller separation by an amount Δf. A second result of this shift will be a decrease in the force constant g, which connects first neighbours to fourth neighbours, by an amount $|\Delta g|$. No change of transverse force constant is allowed for in this model; its effect is expected to be small, as the transverse force constant is only about 10% of the longitudinal. The largest shifts of equilibrium position will be those of the six first neighbours of the samarium ion; these are the only ones taken into account in this model for deformation, and the shifts are all assumed to be the same. Note, however, that shifts in equilibrium position which are negligible from the point of view of lattice symmetry, can cause non-negligible changes in force constants because of the strong dependence of the inter-ionic forces on interionic separation. Thus, it will not be inconsistent to assume that the equilibrium positions may be approximated as being unshifted, but the force constants changed.

As was discussed in Chapter 3, no attempt has been made to include the effect of the vacancy. As a first approximation, this neglect of the vacancy is probably a good approximation. For, provided the vacancy is several neighbours away from the samarium ion, and that its effect on the lattice around it is a short-range distortion (similar to that discussed here for the samarium), the samarium will see the disturbed vacancy region but a larger unperturbed region because of the long range nature of the coupling.

Under the above assumptions, $\underline{\underline{\Gamma}}$ is vastly simplified, and is block diagonal with $\underline{\underline{\Gamma}}_{xx} = \underline{\underline{\Gamma}}_{yy} = \underline{\underline{\Gamma}}_{zz}$, and $\underline{\underline{\Gamma}}_{\alpha\beta} = 0$ for $\alpha \neq \beta$.

The matrix $\underline{\underline{\Gamma}}_{xx}$, in the subspace where it has non-zero elements, is:

$$\underline{\underline{\Gamma}}_{xx} = \begin{bmatrix} \frac{\Delta g}{M_1} & -\frac{\Delta g}{M} & 0 & 0 & 0 \\ -\frac{\Delta g}{M} & \frac{\Delta f+\Delta g}{M_2} & -\frac{\Delta f}{M} & 0 & 0 \\ 0 & -\frac{\Delta f}{M} & \frac{2\Delta f}{M_1} - \lambda\omega^2 & -\frac{\Delta f}{M} & 0 \\ 0 & 0 & -\frac{\Delta f}{M} & \frac{\Delta f+\Delta g}{M_2} & -\frac{\Delta g}{M} \\ 0 & 0 & 0 & -\frac{\Delta g}{M} & \frac{\Delta g}{M_1} \end{bmatrix} \qquad (20)$$

Here, $M = \sqrt{M_1 M_2}$ and $\lambda = (M' - M_1)/M_1$. The rows and columns of this matrix are labelled in the defect space, along the x-direction. The central index refers to the Sm^{++} ion ($\underline{R}_{L\kappa} = 0$, $\kappa = 1$); the indices flanking this to the first neighbours along the x axis ($\underline{R}_{L\kappa} = \pm(a/2)\hat{\underline{i}}$, $\kappa = 2$); and the outer indices to the fourth neighbours ($\underline{R}_{L\kappa} = \pm a\hat{\underline{i}}$, $\kappa = 1$). The row and column labels in this space will be abbreviated as $\bar{2}x$, $\bar{1}x$, $0x$, $1x$, $2x$; and the subscripts (ℓka) or $(\ell' k' b)$ will be used to label elements in the 15×15 defect space.

D. Calculation of the sideband spectrum

The spectrum is given by equation 19. This can be written, and most easily calculated, in two parts:

$$W(\omega) = W^\circ(\omega) - W'(\omega) \qquad (21)$$

where $W^\circ(\omega)$ is the unperturbed transition probability and $W'(\omega)$ is a correction term giving the effect of the lattice perturbation.

$W^\circ(\omega)$ is given by

$$W^\circ(\omega) = \mathrm{Im} \sum_{\substack{L\ \kappa\ \alpha \\ L'\kappa'\beta}} \frac{\Phi^{C}_{x\alpha}(0L;1\kappa)}{\sqrt{M_\kappa}}\, G^\circ_{L\kappa\alpha,L'\kappa'\beta}(\omega)\, \frac{\Phi^{C}_{\beta x}(L'0;\kappa'1)}{\sqrt{M_{\kappa'}}}$$

$$= \frac{16}{N} \sum_{\substack{\underline{q}j \\ \beta}}{}' \left\{ \sum_{\kappa\alpha} \frac{\overset{1\kappa}{\underset{q}{C(\beta\alpha)}}\ \xi_\alpha(\kappa\underline{q}j)}{\sqrt{M_\kappa}} \right\}^2 \frac{\pi}{2\omega_{\underline{q}j}}\ \delta(\omega_{\underline{q}j} - \omega), \qquad (22)$$

where $\sum'_{\underline{q}j}$ means the sum is restricted to the irreducible 1/48th of the Brillouin zone.

$W'(\omega)$ can be written

$$W'(\omega) = \mathrm{Im} \sum_{\substack{\ell k a \\ \ell' k' b}} V_{\ell ka}(\omega)\, T_{\ell ka, \ell' k' b}(\omega)\, V_{\ell' k' b}(\omega) \,, \tag{23}$$

where the summation runs over the elements of the defect space as given in the previous section. Here $V_{\ell ka}(\omega)$ has been defined as

$$V_{\ell ka}(\omega) = \frac{1}{N} \sum_{L\kappa\alpha} \frac{\Phi^{C}_{x\alpha}(0L;1\kappa)}{\sqrt{M_\kappa}}\, G^{\circ}_{L\kappa\alpha,\ell ka}(\omega)$$

$$= \frac{1}{N} \sum_{\substack{\kappa\alpha \\ \underline{q}j}} \frac{C^{1\kappa}_{\underline{q}}(x\alpha)}{\sqrt{M_\kappa}}\, \xi_\alpha(\kappa\underline{q}j)\, \xi_a(k\underline{q}j)\, \exp(-i\underline{q}\cdot\underline{R}_{\ell k})\, G^{\circ}_{\underline{q}j}(\omega)$$

$$= \frac{16}{N} \sum_{\substack{\underline{q}j \\ \beta}}{}' \sum_{\kappa\alpha} \frac{C^{1\kappa}_{\underline{q}}(\beta\alpha)}{\sqrt{M_\kappa}}\, \xi_\alpha(\kappa\underline{q}j)\, \xi_a(k\underline{q}j) \quad \cos(\underline{q}\cdot\underline{R}_{\ell k})\, G^{\circ}_{\underline{q}j}(\omega)\,\delta_{a\beta}\,. \tag{24}$$

In writing the final lines of both equation 22 and equation 24 use has been made of the symmetry of the equation for the whole Brillouin zone.

In the defect space as defined for Γ in section C, $V_{\ell ka}(\omega)$ has $T_{1u}{}^{x}$ symmetry. It is thus convenient to transform partly to the "cubic symmetry space" as mentioned in Chapter 3. The transformation $\underline{\mathcal{D}}_1$, given in Appendix A, separates $\underline{\Gamma}$ and G° into even and odd parity blocks; in this basis, $\underline{V}$ has only 3 non-zero elements corresponding to the 3 possible $T_{1u}{}^{x}$ motions of the ions in the defect space:

$$\begin{aligned} V_2 &= \frac{1}{2}\,(V_{2x} + V_{\bar{2}x}) \\ V_1 &= \frac{1}{2}\,(V_{1x} + V_{\bar{1}x}) \qquad\qquad (25) \\ V_0 &= V_{0x}\ . \end{aligned}$$

The $T_{1u}{}^{x}$ block of $\underline{\underline{\Gamma}}$ is of the form

$$\begin{bmatrix} \Delta g/M_1 & -\Delta g/M & 0 \\ -\Delta g/M & \dfrac{(\Delta f+\Delta g)}{M_2} & -\sqrt{2}\Delta f/M \\ 0 & \sqrt{2}\Delta f/M & \dfrac{2\Delta f}{M_1} - \lambda\omega^2 \end{bmatrix}, \qquad (26)$$

while that of G° is

$$\begin{bmatrix} g_{22} & g_{12} & g_{02} \\ g_{12} & g_{11} & g_{01} \\ g_{02} & g_{01} & g_{00} \end{bmatrix}, \qquad (27)$$

with

$$g_{00} = \frac{1}{N} \sum_{\underline{q}j} \frac{\xi_x{}^2(1\underline{q}j)}{\omega_{\underline{q}j}^2 - \omega^2} \equiv \frac{16}{N} \sum_{\substack{\underline{q}j \\ \alpha}}{}' \frac{\xi_\alpha{}^2(1\underline{q}j)}{\omega_{\underline{q}j}^2 - \omega^2}$$

$$g_{11} = \frac{2}{N} \sum_{\underline{q}j} \frac{\xi_x{}^2(2\underline{q}j)\cos^2(q_x a/2)}{\omega_{\underline{q}j}{}^2 - \omega^2}$$

$$g_{22} = \frac{2}{N} \sum_{\underset{\sim}{q}j} \frac{\xi_x^{\,2}(1\underset{\sim}{q}j)\cos^2(q_x a)}{\omega_{\underset{\sim}{q}j}^{\,2}-\omega^2} \tag{28}$$

$$g_{01} = \frac{\sqrt{2}}{N} \sum_{\underset{\sim}{q}j} \frac{\xi_x(1\underset{\sim}{q}j)\ \xi_x(2\underset{\sim}{q}j)\cos(q_x a/2)}{\omega_{\underset{\sim}{q}j}^{\,2}-\omega^2}$$

$$g_{02} = \frac{\sqrt{2}}{N} \sum_{\underset{\sim}{q}j} \frac{\xi_x^{\,2}(1\underset{\sim}{q}j)\cos(q_x a)}{\omega_{\underset{\sim}{q}j}^{\,2}-\omega^2}$$

$$g_{12} = \frac{2}{N} \sum_{\underset{\sim}{q}j} \frac{\xi_x(1\underset{\sim}{q}j)\ \xi_x(2\underset{\sim}{q}j)\cos(q_x a/2)\cos(q_x a)}{\omega_{\underset{\sim}{q}j}^{\,2}-\omega^2} .$$

The $T_{1u}{}^{x}$ part of the matrix $\underline{\underline{T}}$ can be found from these two matrices.

The imaginary parts of $\underline{V}$ can be found using the usual method of sorting into "bins" in frequency, and their real parts by integration as described by Timusk and Klein (1966), using the fact that

$$\mathrm{Re}\ V(\omega) = \frac{2}{\pi} \int_0^\infty \frac{\mathrm{Im}\ V(s)}{s^2 - \omega^2}\, s\, ds; \tag{29}$$

$\underline{\underline{T}}(\omega)$ can be found using the elements of $\underline{\underline{G}}^\circ$ as found in this manner.

The calculations were carried out by constructing a histogram with 100 bins in frequency over the range of phonon frequencies. Shell Model VI phonons (Cowley et al. 1963) for 1686 values of $\underset{\sim}{q}$ in 1/48th of the Brillouin zone were used; for KBr, the shell model parameters of Cowley et al. (1963), were used, and for KCl those of Copley et al., (to be published). The values of Δf and Δg were varied between $-f$ and $+f$ and $-g$ and $+g$, respectively, to find the best fit to experiment.

E. Comparison with experiment and discussion

Figure 9 shows the calculation $W^{\circ}(\omega)$ compared with a sketch of the experimental sideband for KBr. The relative scales of the two curves are chosen arbitrarily. This unperturbed calculation agrees well with the experimental curve in the relative strengths of the accoustical and optical branches, and all the major peaks in the experimental curve are represented and agree quite closely in shape. A sharp and strong phonon peak at 132 cm^{-1} in the density of states calculated from the shell model is missing in the calculated sideband, as in the experiment.

There are, however, several discrepancies between the calculation $W^{\circ}(\omega)$ and the experiment. The sharp peak at 93 cm^{-1} does not appear in the calculation, nor does the "hook" at 40.5 cm^{-1}. The agreement in the lower part of the optic branch is not good since there is basically only a single peak in the calculation, while the experiment shows a double peak.

Figure 10 shows the perturbed calculation,

Figure 9. The unperturbed calculation ($W_o(\omega)$) for the sideband of KBr:Sm^{++} compared with the experimental sideband. The relative scale of the two curves has been chosen arbitrarily. A smooth curve has been drawn through the centre of the histogram contributions for the theoretical curve. The arrows indicate the frequencies observed accompanying $4f^6 \rightarrow 4f^5 5d$ transitions.

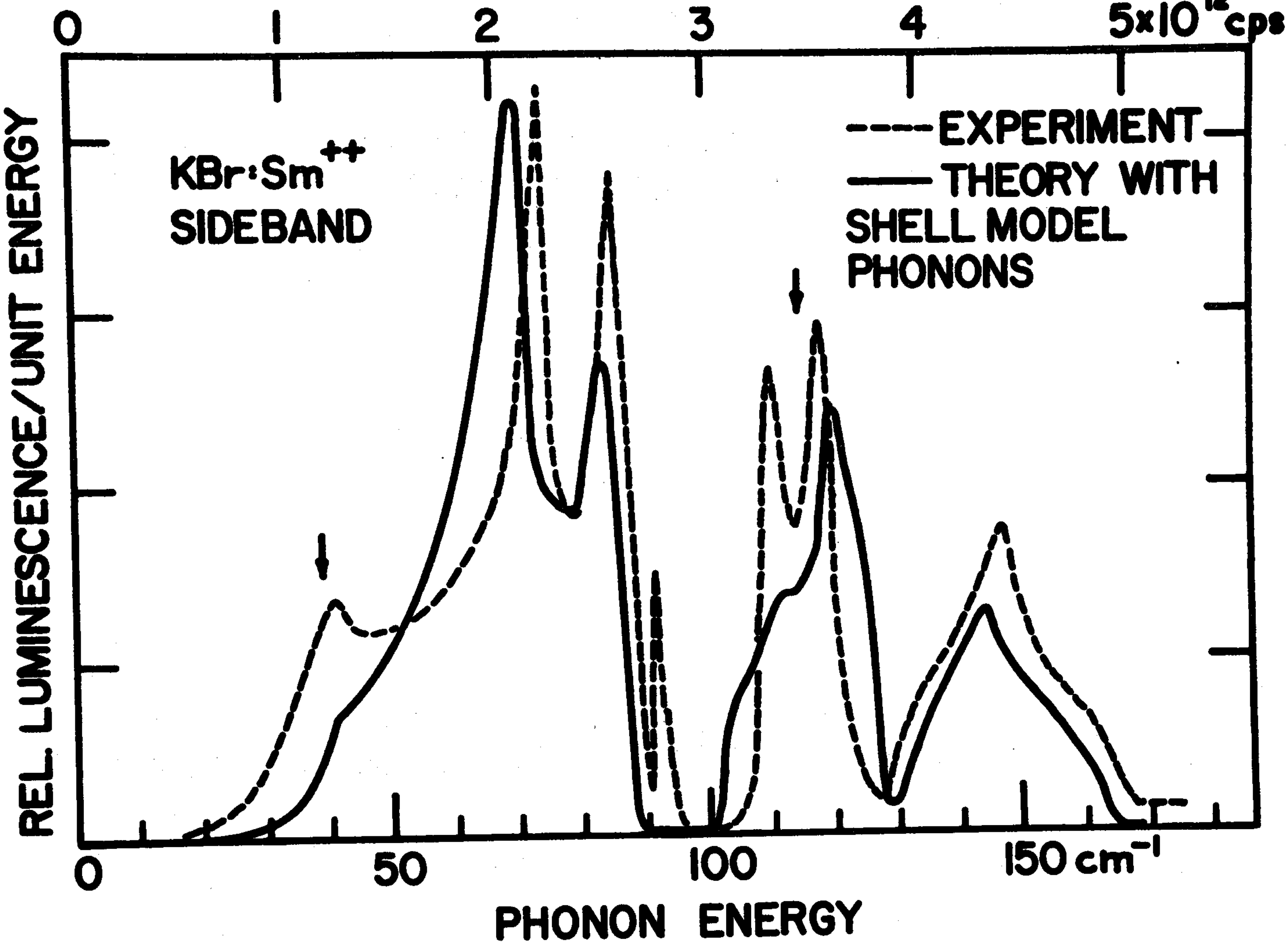
0
1
2
3
4
5x10^{12}cps
KBr:Sm^{++}
SIDEBAND
----EXPERIMENT
—— THEORY WITH
SHELL MODEL
PHONONS
REL. LUMINESCENCE/UNIT ENERGY
0
50
100
150 cm^{-1}
PHONON ENERGY

Figure 10. The perturbed sideband ($W(\omega)$) for Sm^{++} in KBr, for the lattice deformation discussed with $\Delta f = +14500$ dynes/cm and $\Delta g = -1500$ dynes/cm, compared with the experimental sideband. The relative scale of the curves has been chosen arbitrarily.

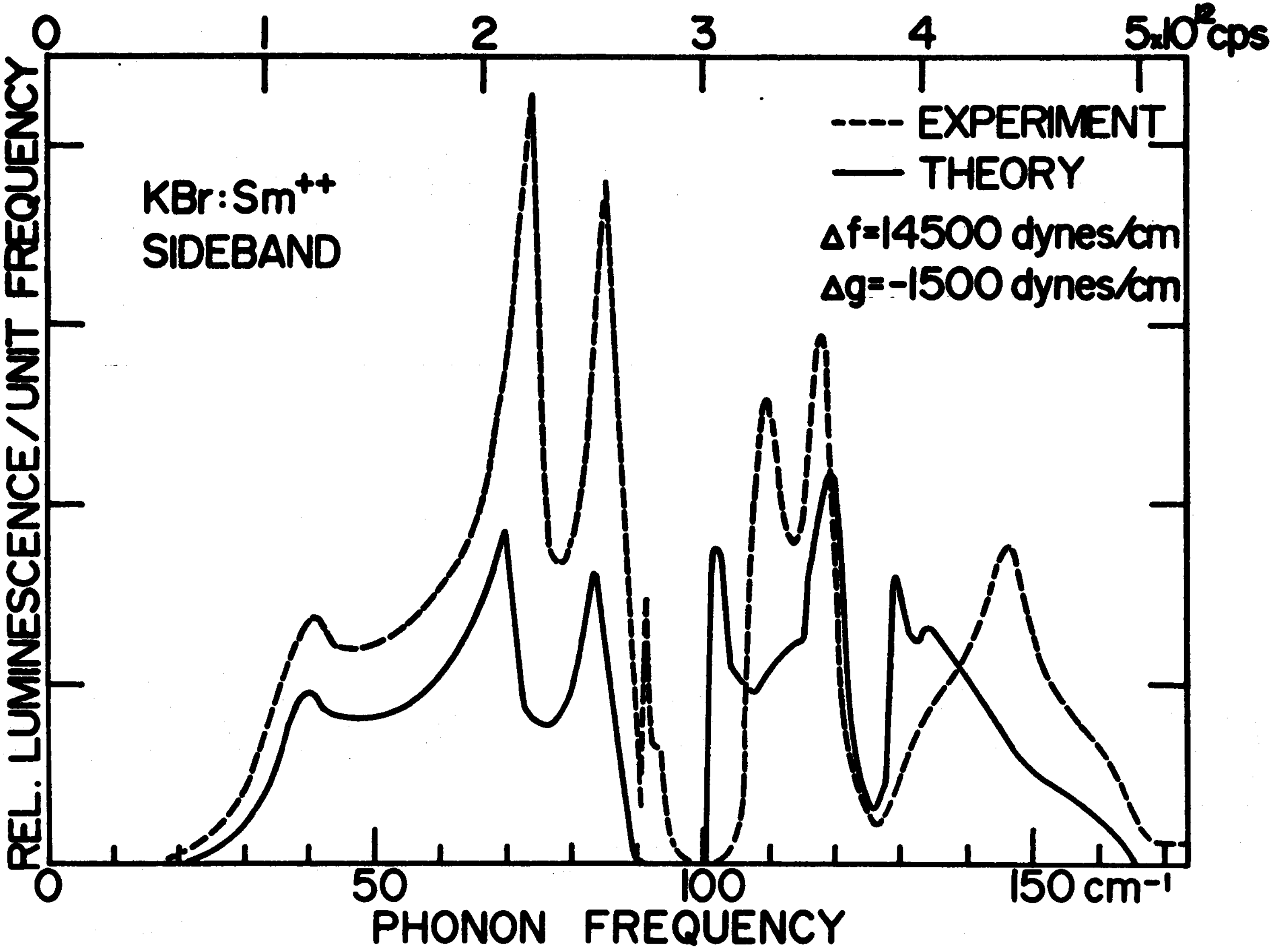

0
1
2
3
4
5x10¹²cps
---- EXPERIMENT
—— THEORY
KBr:Sm⁺⁺
SIDEBAND
Δf=14500 dynes/cm
Δg=-1500 dynes/cm
REL. LUMINESCENCE/UNIT FREQUENCY
0
50
100
150 cm⁻¹
PHONON FREQUENCY

$$W(\omega) = W^{\circ}(\omega) - W'(\omega),$$

for KBr:Sm^{++} for Δf = 14500 dynes/cm and Δg = -1500 dynes/cm. The relative scale of the experimental and theoretical plots was again chosen arbitrarily, but is very closely the same as for figure 9 .

This curve shows improved agreement in two of the regions of poor agreement for the unperturbed calculation. Change of the mass at the origin gives rise to the "hook" at 41 cm^{-1}; its position and shape are independent of the force constant changes. The changes Δf and Δg in the force constants can be picked to give a double peak in the transverse optic region.

The lowered intensity for the peaks at 70 cm^{-1} and 83 cm^{-1} is probably not significant, as these peaks are known from calculations of density of states with a larger sampling of points (Cowley and Cowley 1966) to be stronger and sharper than represented by the smaller sample of $\underline{q}$'s used here.

The fit in the longitudinal optic region is uniformly poor with this model of $\underline{\underline{\Gamma}}$, for all force constant changes. The peak at 129 cm^{-1} occurs where the fifth and sixth phonon branches overlap in frequency. Thus, it is not clear whether the poor fit is an indication that the phonons used are not sufficiently accurate for a calculation such as this which depends strongly on the eigenvectors, or is due to the simplicity of the model used for the lattice perturbation. It should be mentioned, however, that the agreement in the optic region is very much poorer if only the mass change is made ($\Delta f = \Delta g = 0$), or if only the mass change and the force constant change Δf are allowed for. In these cases, although the acoustic branch remains similar, the optic branch shows very low intensity in the transverse optic region (100 cm^{-1} to 125 cm^{-1}), and a very strong peak at 129 cm^{-1}. The fact that the more extensive $\underline{\underline{\Gamma}}$ with two force constant changes gives so much better agreement than these cases would appear to be a suggestion that the deformation of the lattice about the samarium ion may be more extensive than has been allowed for here, and that improved agreement could be obtained with a yet more extensive $\underline{\underline{\Gamma}}$.

The apparently good agreement of the unperturbed sideband calculation, $W°(\omega)$, seems to be somewhat fortuitous. The discrepancies are small, and occur where they are somewhat masked by other features: the "hook" at 40.5 cm^{-1} is not particularly pronounced, and occurs approximately at the frequency of the Van Hove singularity in the calculated curve, while the double peak in the transverse optic region seems to be at least indicated in the calculation. However, it appears from studies of other sidebands in both absorption and fluorescence for KBr systems containing Sm^{++} that both these regions in frequency are affected by the local deformation (Wagner and Bron 1965).

Figures 11 and 12 show the unperturbed and perturbed calculations, respectively, for $KCl:Sm^{++}$, compared with a sketch of the experimental curve. The relative scale is again chosen arbitrarily, and is the same in both curves. The perturbed calculation has been made with $\Delta f = +14500$ dynes/cm and $\Delta g = -1500$ dynes/cm. For this host lattice, the agreement of the unperturbed calculation with experiment is less good; the rounded peak at 53 cm^{-1} is absent in the calculation, and the rest of the features, with the exception of the sharp peak at 155 cm^{-1}, are not in good agreement, being shifted in frequency and different in shape and intensity.

For KCl, the perturbed calculation shows marked improvement over the unperturbed calculation; it brings in the rounded peak at 53 cm^{-1} and changes the relative intensities of the peaks. The peak centering around 117 cm^{-1} is much weaker than observed, but agrees more closely in shape in the perturbed sideband calculation. The last experimental peak, at 168 cm^{-1},does not appear in either calculation, while the peak at 155 cm^{-1} is, in this calculation, much too strong: its maximum strength is about 1.5 times that of the experimental peak on the scales plotted. Some of this discrepancy is, however, due to the neglect of the photomultiplier and spectrometer response correction, which would raise the in-

Figure 11. The unperturbed calculation ($W_o(\omega)$) for KCl:Sm^{++} compared with the experimental sideband. The relative scale of the two curves has been chosen arbitrarily.

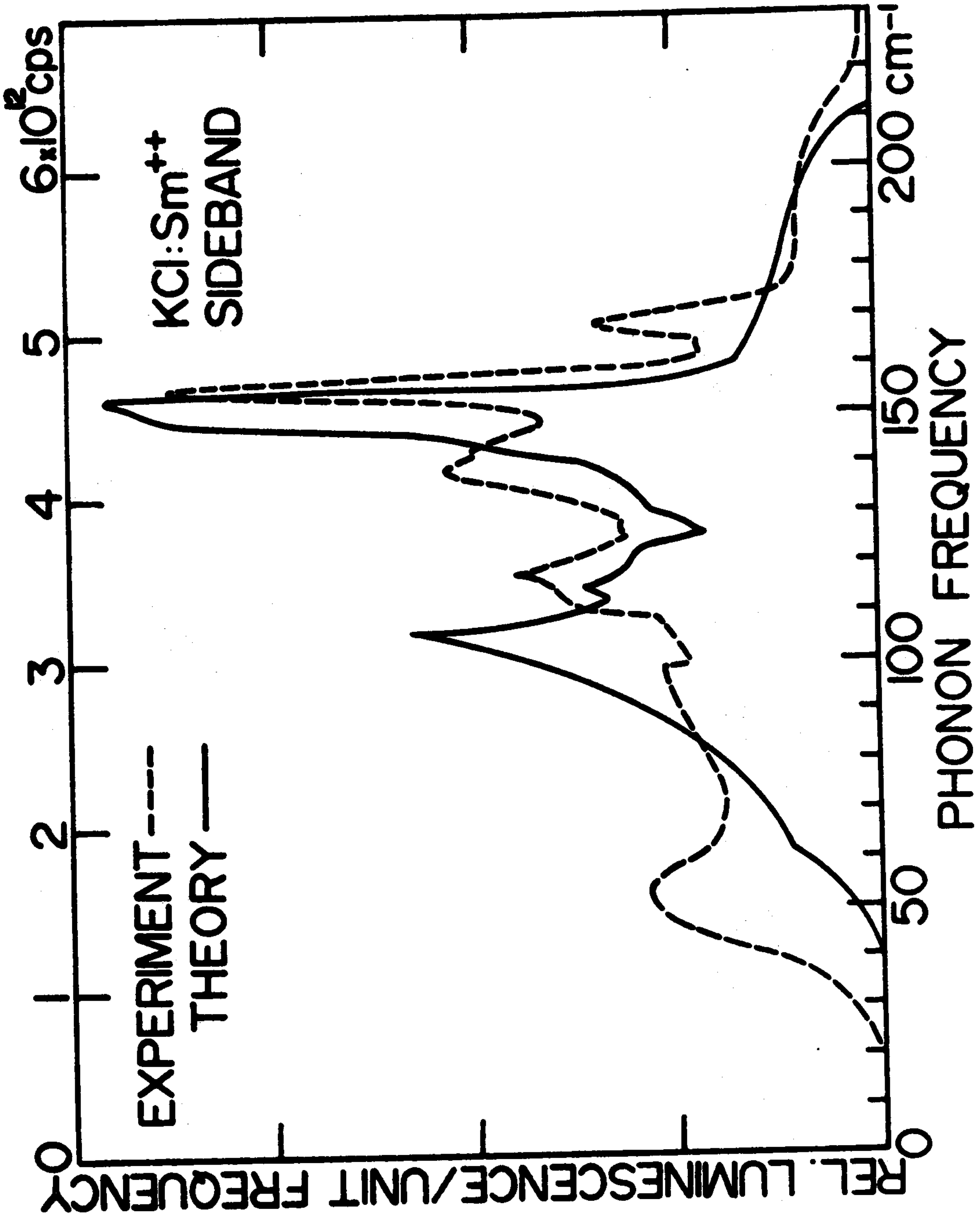
KCl:Sm++
SIDEBAND
EXPERIMENT ----
THEORY ——
REL. LUMINESCENCE/UNIT FREQUENCY
PHONON FREQUENCY
0
1
2
3
4
5
6x10¹² cps
0
50
100
150
200 cm⁻¹

Figure 12. The perturbed sideband calculation ($W(\omega)$) for $KCl:Sm^{++}$ for the lattice deformation discussed with $\Delta f = +14500$ dynes/cm and $\Delta g = -1500$ dynes/cm, compared with the experimental sideband. The peak at 155 cm^{-1} is asymmetric as in the unperturbed calculation; its strength is 1.5 times that of the experimental peak on the plotted scale. The curves are plotted on the same scales as those of figure 11.

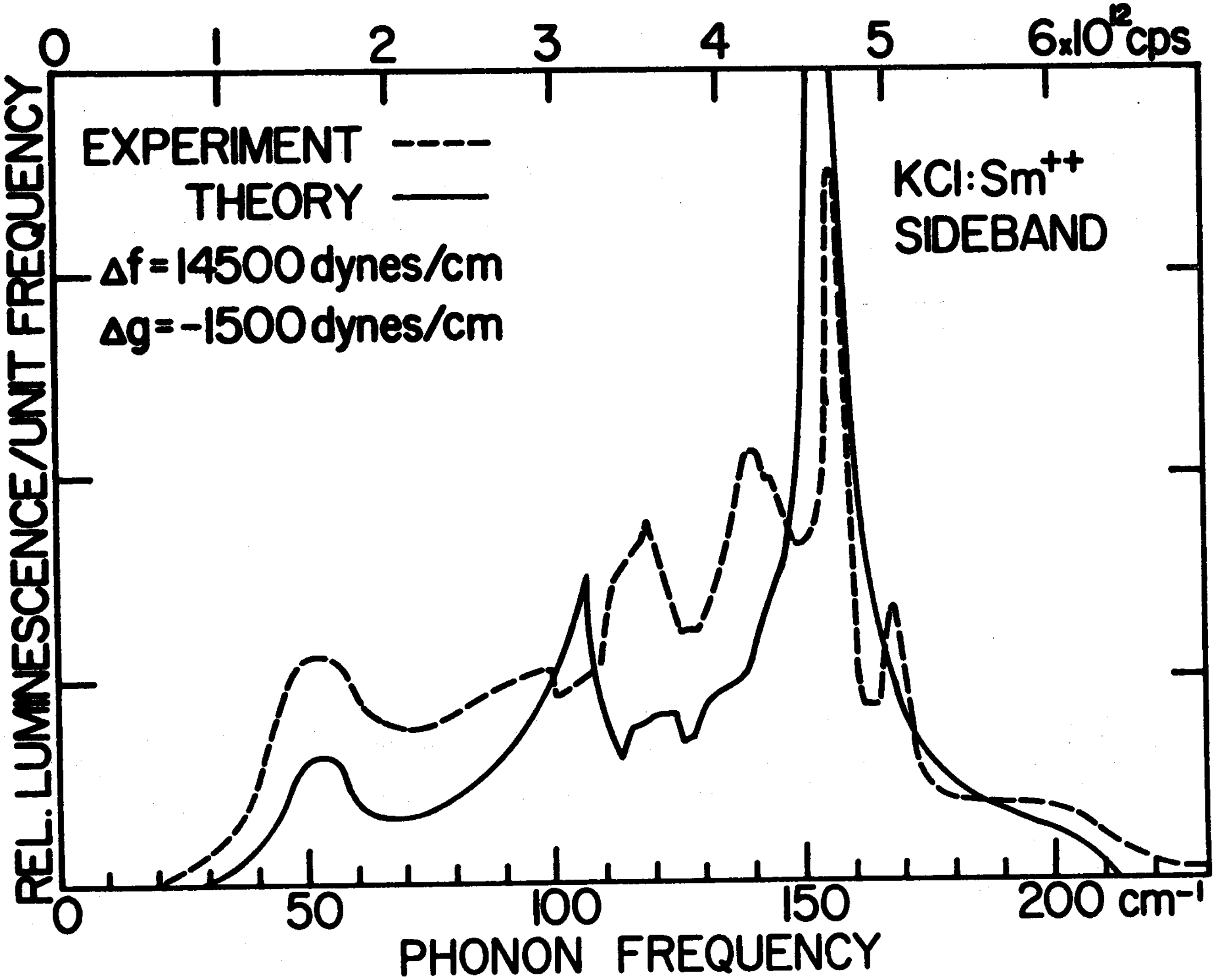
0
1
2
3
4
5
6x10¹²cps
EXPERIMENT ----
THEORY ——
Δf=14500 dynes/cm
Δg=-1500 dynes/cm
KCl:Sm++
SIDEBAND
REL. LUMINESCENCE/UNIT FREQUENCY
0
50
100
150
200 cm-1
PHONON FREQUENCY

tensity of the 155 cm^{-1} peak by 20%, as compared with the rounded peak at 53 cm^{-1}.

In the KCl perturbed calculation, the rounded peak at 53 cm^{-1} is again the result of the changed mass at the origin and is independent of the force constant changes made. The peak at 155 cm^{-1} is a resonance; its position, intensity, and width are dependent on the size of Δf and Δg. While it is not as sensitive to changes in Δf and Δg as are the peaks in the transverse optic region for KBr, the best fit in frequency is found for force constant changes about the same as for KBr.

Some of the other discrepancies between the calculated curves and the experimental curves can be understood in terms of limitations of the shell model phonons. The "step" at 106 cm^{-1} in the calculation for KCl is seen in the experiment at 100 cm^{-1}; this 6% discrepancy should be compared to the discrepancy between the analogous peaks (at 70 cm^{-1} and 74.7 cm^{-1} respectively) in the calculations and experiments for KBr. In both cases these features correspond to a saddle point in the second accoustical branch. The saddle point arises from a region in the Brillouin zone not measured by neutron diffraction, in the (110) plane; for $\underline{q}$ from approximately $\frac{2\pi}{a}(.5,.5,0)$ to $\frac{2\pi}{a}(5,.5,.5)$ the frequency is almost constant, and slightly below the maximum frequency of that branch. Along this line the eigenvectors are normal to the plane, and the light ion is almost motionless for KBr; for KCl the lighter ion also moves somewhat. This saddle point does not seem to be particularly well represented in Shell Model VI; the phonons actually measured by neutron diffraction near this region fall at lower frequencies than those predicted for KCl; while for KBr they seem to fall at higher frequencies. In both cases this is in better agreement with the Sm^{++} sideband experimental results.

It should also be pointed out that a completely similar saddle point exists in the optic branch: it arises from the same range of $\underline{q}$, and for KBr at least corresponds to the heavy ions being motionless and eigenvectors normal to the (110) plane. This region gives rise to the lower saddle point in the fourth branch. The maximum intensity in the density of states of the fourth phonon branch occurs at about 140 cm^{-1} for KCl and at 111 cm^{-1} for KBr. Peaks are observed experimentally at these frequencies in KCl and KBr respectively, but no peak shows up in either the calculations or the density of states used. It is thus a possibility that the shell model is not giving the correct solutions in this region, as well as in the similar region of the accoustic branch.

Finally, it should be mentioned that the shell model phonons used were for a temperature of 90°K, while the experiments were done at 7°K. As was shown by Woods et al.(1963), the shift in frequencies as a result of the temperature may amount to a decrease of as much as 8% between 400°K and 90°K; so one might expect that there exists a possible 2% error in some of the phonon frequencies used.

Some of the remaining discrepancies between the calculated sidebands and the experimental sidebands that cannot be assigned to the shell model predictions must be assumed to arise as a result of the simplicity of the lattice perturbation model used. The assumption of cubic site symmetry for the samarium ion, while good as a first approximation, may not give all the features of the sideband, and may be responsible for the poor agreement obtained in the optical branch of the $KBr:Sm^{++}$ curve. The deformation probably extends further than the first neighbours of the impurity, and the approximation of unchanged equilibrium positions may not be good. However the fact that this model gives fairly good overall agreement indicates that all the assumptions made in performing this calculation are fairly good, although more complicated models for $\underline{\underline{\Gamma}}$ allowing for more force constant changes, or models allowing for a non-cubic environment might well be expected to give better agreement.

F. Other work supporting the model for the samarium sideband

The results of some other calculations can be mentioned to give further support to both the mechanism chosen for the coupling and the model for Γ used.

On this mechanism for the coupling, the intensity of the zero-phonon line can be calculated and compared with the one phonon intensity, for various positions of the vacancy. The transition rate for the zero phonon line is given by

$$W_{e\rightarrow g}(0) = \frac{2\pi}{\hbar} \left|\sum_i \left\{\frac{<\chi^0\phi_g|H_p|\chi^0\phi_i><\chi^0\phi_i|H_s|\chi^0\phi_e>}{\varepsilon_i - \varepsilon_e}\right.\right.$$

$$\left.\left. + \frac{<\chi^0\phi_g|H_s|\chi^0\phi_i><\chi 0\phi_i|H_p|\chi^0\phi_e>}{\varepsilon_i - \varepsilon_e}\right\}\right|^2$$

$$\times\ \delta(\varepsilon_g + \hbar\omega_p - \varepsilon_e) \qquad (30)$$

$$= \frac{\Delta\Omega\omega_o\ \Delta\omega}{2\pi\hbar c^3}\ e^2\ \left|\sum_i <\phi_g|r_x|\phi_i><\phi_i|r_x|\phi_e>\right.$$

$$\left.\times\ \left\{\frac{\varepsilon_i-\varepsilon_g}{\varepsilon_i-\varepsilon_e} + \frac{\varepsilon_e-\varepsilon_i}{\varepsilon_i-\varepsilon_g}\right\}\right|^2 \frac{\hbar}{\pi}\ W(0) \qquad (31)$$

for electric dipole radiation. These equations can be compared with equations 5 and 15. In writing equation 31, H_s has been written

$$H_s = \frac{e^2}{|R_v+r|} = \frac{e^2}{|R_v|}\ \{1 - \frac{R_v \cdot r}{R_v^2} + \ .....\} \qquad (32)$$

and the term linear in $\underline{r}$ kept. $\underline{R}_v$ is the position of the vacancy. Thus,

$$W(0) = \frac{\pi}{h}\,\frac{1}{3}\sum_{\alpha}\left[\frac{R_{v\alpha}}{|\underline{R}_v|^3}\right]^2 \delta(\omega) \quad ; \qquad (33)$$

an average has been taken over photon polarizations.

The intensity predicted for the zero phonon line, $I_0 = \int W(0)\, d\omega$ can then be directly compared with that predicted for the one-phonon sideband, $I_1 = \int W(\omega)\, d\omega$, from equation 16. Experimentally, the ratio I_1/I_0 has been determined to be 0.40 for KBr:Sm^{++}. For a vacancy at (a/2,a/2,0), the calculated ratio is 0.06, only 15% of the observed ratio. A vacancy further away gives better agreement, for that would decrease the predicted I_0. This comparison then supports the assumption of a relatively distant vacancy. Note, however, that this is only a rough estimate of I_0 since the relaxation of the lattice has not been allowed for.

The low frequency ω-dependence can also be compared with that observed. For the calculated sideband,

$$W(\omega) \propto \sum_{\underline{q}j}\left[\sum_{L\kappa\alpha}\Phi^{C}_{x\alpha}(0L;l\kappa)\,\xi_\alpha(\kappa\underline{q}j)\exp(i\underline{q}\cdot\underline{R}_{L\kappa})\right]^2 \frac{\delta(\omega_{\underline{q}j}-\omega)}{\omega}$$

$$= \sum_{\underline{q}j}\left[\sum_{L\kappa\alpha}\Phi^{C}_{x\alpha}(0L;l\kappa)\,\xi_\alpha(\kappa\underline{q}j)\cos(\underline{q}\cdot\underline{R}_{L\kappa})\right]^2 \frac{\delta(\omega_{\underline{q}j}-\omega)}{\omega}$$

$$= \sum_{\underline{q}j}\left[\sum_{L\kappa\alpha}\Phi^{C}_{x\alpha}(0L;l\kappa)\,\xi_\alpha(\kappa\underline{q}j)(\cos(\underline{q}\cdot\underline{R}_{L\kappa})-1)\right]^2 \frac{\delta(\omega_{\underline{q}j}-\omega)}{\omega}, \qquad (34)$$

since $\sum_{L}\Phi^{C}_{x\alpha}(0L;l\kappa) = 0$.

At low ω, only the acoustic branches enter, and $\omega_{qj} = v_j q$; thus, $(\cos(\underline{q}\cdot\underline{R}_{LK})-1)$ is proportional to ω^2 for low ω. The number of terms contributing in this region is proportional to the density of states, which is proportional to ω^2 at low ω. Thus, $W(\omega) \propto \omega^5$ in the low frequency region*. This discussion of frequency dependence will apply equally well for the perturbed lattice if no resonant modes are introduced in the low frequency region.

This predicted frequency dependence agrees with that observed for both KBr:Sm^{++} and KCl:Sm^{++} as shown by figure 13.

Finally, this model for $\underline{\underline{\Gamma}}$ has been used in the calculation of the infrared absorption of KBr:Sm^{++} crystals, as done by Woll et al. (1968). The calculated infrared absorption, using the same force constants as used for the sideband, is compared with experiment in figure 14. The peaks B and C are shifted from their predicted positions by the same amounts as observed in fluorescence, but good overall agreement is seen between experiment and theory.

---

*This frequency dependence, and that for sidebands of even→odd transitions as discussed in Chapter 5, appears to have been first pointed out by Louden: see the paper of Hobden, 1965.

Figure 13. The low frequency ω-dependence for both $KBr:Sm^{++}$ and $KCl:Sm^{++}$ sidebands. The theoretical ω-dependence would give a slope of 5; the dashed lines, extending the straight-line portion of the experimental curve show a slope of 4.9 for $KBr:Sm^{++}$ and of 4.8 for $KCl:Sm^{++}$. The experimental curves deviate from these lines at the high frequency end because the dispersion curves have ceased to be linear with ω; and at the low frequency end because of the tail of the zero-phonon line.

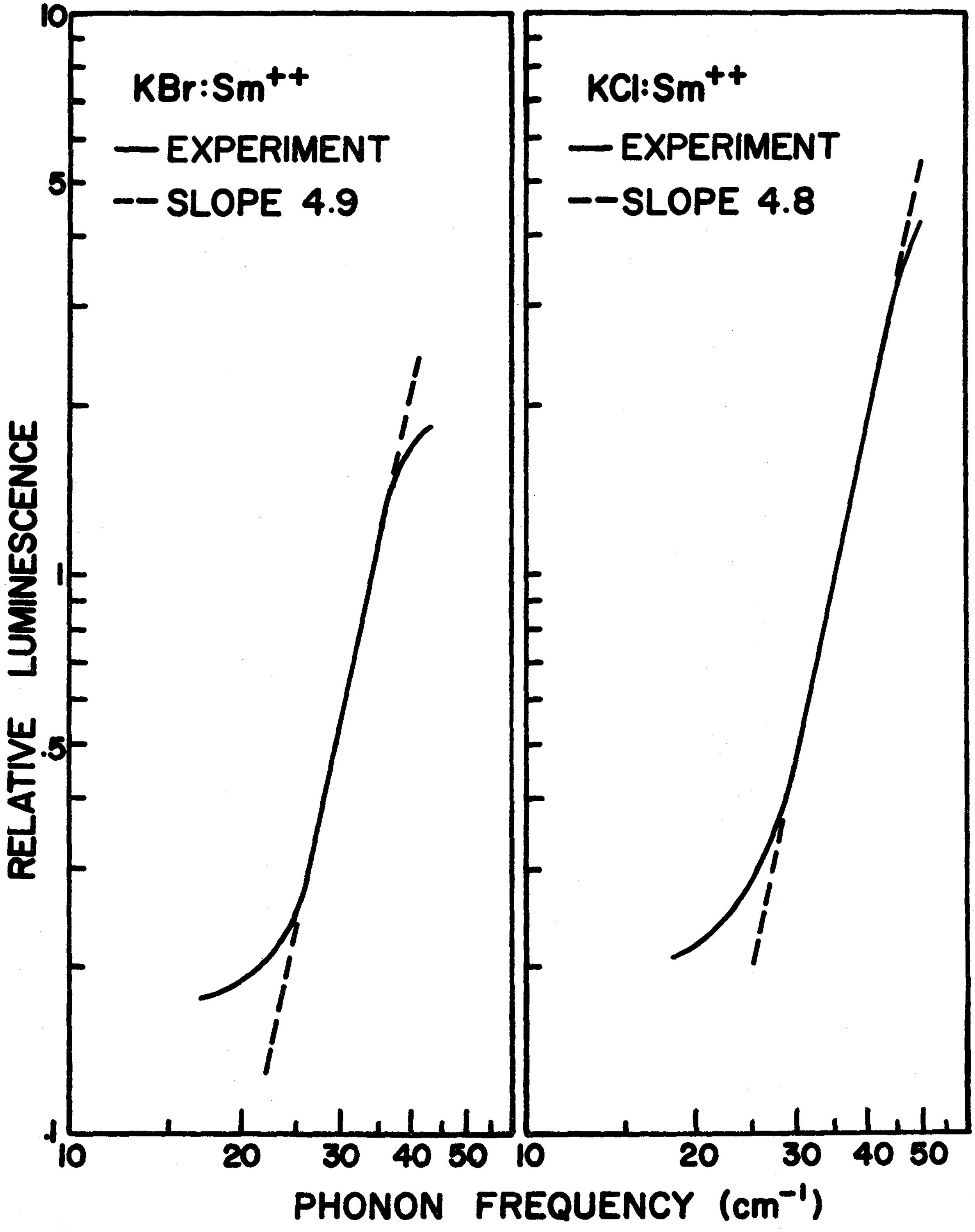
KBr:Sm^{++}
— EXPERIMENT
-- SLOPE 4.9
KCl:Sm^{++}
— EXPERIMENT
-- SLOPE 4.8
RELATIVE LUMINESCENCE
10
5
1
.5
.1
10
20
30
40
50
10
20
30
40
50
PHONON FREQUENCY (cm^{-1})

Figure 14. The far infrared absorption of $KBr:Sm^{++}$ (.01 at.%), compared with the theoretical calculation of the infrared absorption. The calculation was made with the same model of the lattice perturbation as used for the sideband shown in figure 10 (Δf = 14500 dynes/cm, Δg = -1500 dynes/cm), and is plotted on an arbitrarily chosen scale. The peaks B and C observed in the sideband are labelled; the same shift in frequency from the calculated peaks is observed here. The resolution for the experimental curve is .11 cm^{-1}. The peak at 95 cm^{-1} is due to Cl^-. The experimental curve was taken by R. W. Ward.

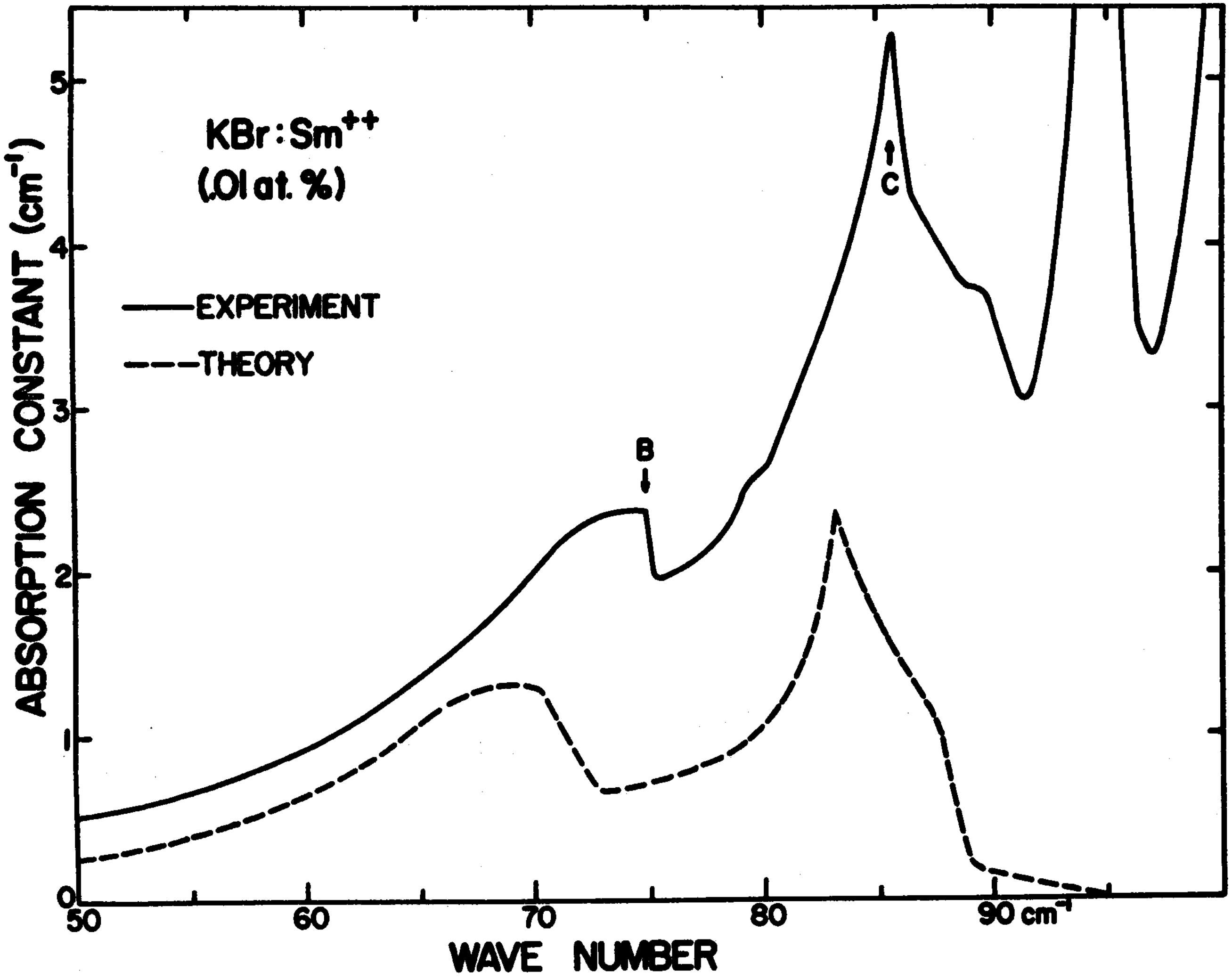
KBr : Sm^{++}
(.01 at. %)
EXPERIMENT
THEORY
B
C
ABSORPTION CONSTANT (cm^{-1})
0
1
2
3
4
5
50
60
70
80
90 cm^{-1}
WAVE NUMBER

CHAPTER 5

SIDEBANDS OF ALLOWED TRANSITIONS

The transition between two states of even parity, that is involved for the sidebands discussed in the preceding chapters, is a special case. For many other systems, the electronic transition is one between levels of opposite parity. Examples of this are the systems of Sm^{++} or Eu^{++} in CaF_2 (Runciman and Stager 1962;1963), or Eu^{++} in alkali halides (Wagner and Bron 1965). The transition probability for these sidebands can be written under the same assumptions as made for the problem of samarium in alkali halides.

The discussion will be carried out from the point of view of Sm^{++} or Eu^{++} in CaF_2, where the symmetry is still cubic.

For such a sideband the terms in H_Q of interest are those in even powers of $\underline{r}$; for the sideband transition probability,

$$W_{e\to g}(\omega) = \frac{2\pi}{\hbar} \sum_{\substack{\text{final}\\ \text{states}}} \left| \sum_{i} \frac{\langle\Psi_g|H^I|\Psi_i\rangle\langle\Psi_i|H^I|\Psi_e\rangle}{E_i - E_e} \right|^2 \times \delta(E_g - E_e)$$

$$= \frac{2\pi}{\hbar} \sum_{\substack{\text{final} \\ \text{states,} \\ \{p,q\}}} \left| \sum_{i} \left\{ \frac{<\chi^1\phi_g|H_p|\chi^1\phi_i><\chi^1\phi_i|H_q|\chi^0\phi_e>}{\varepsilon_i + \hbar\omega_{\underset{\sim}{q}} - \varepsilon_e} \right.\right.$$

$$\left.\left. + \frac{<\chi^1\phi_g|H_q|\chi^0\phi_i><\chi^0\phi_i|H_p|\chi^0\phi_e>}{\varepsilon_i + \hbar\omega_{\underset{\sim}{p}} - \varepsilon_e} \right\} \right|^2$$

$$\times\ \delta(\varepsilon_g + \hbar\omega_{\underset{\sim}{q}} + \hbar\omega_{\underset{\sim}{p}} - \varepsilon_e)\ , \qquad (1)$$

involves, in this case, the following electronic matrix elements:

$$<\phi_g(\text{even})|H_p(\text{odd})|\phi_i(\text{odd})><\phi_i(\text{odd})|H_q(\text{even})|\phi_e(\text{odd})> \qquad (2)$$

and

$$<\phi_g(\text{even})|H_q(\text{even})|\phi_i(\text{even})><\phi_i(\text{even})|H_p(\text{odd})|\phi_e(\text{odd})>.(3)$$

Here the parities of the possible intermediate states and of the possible terms in H_q have been written explicitly assuming again that the important contribution comes from the electric dipole terms, where $H_p = eE_x r_x$ (i.e. of $T_{1u}{}^x$ symmetry). The excited state has been assumed to be odd and the ground state even.

The most important terms in the sum over intermediate states are those for which, in (2), ϕ_i is ϕ_e, and, in (3), ϕ_i is ϕ_g; for then the energy denominator of the first $\varepsilon_i + \hbar\omega_{\underset{\sim}{q}} - \varepsilon_e$, becomes just $\hbar\omega_{\underset{\sim}{q}}$, while that of the second, $\varepsilon_i + \hbar\omega_{\underset{\sim}{p}} - \varepsilon_e = \varepsilon_i - \hbar\omega_{\underset{\sim}{q}} - \varepsilon_g$, becomes $-\hbar\omega_{\underset{\sim}{q}}$.

Then equation (1) becomes*

$$W_{e\to g}(\omega) = \frac{2\pi}{\hbar} \sum_{\substack{\text{final} \\ \text{states,} \\ \{p,q\}}} \left| \frac{\langle\phi_g|H_{\underline{p}}|\phi_e\rangle}{\hbar\omega_{\underline{q}}} \{\phi_e\chi^1|H_{\underline{q}}|\phi_e\chi^0\rangle - \langle\phi_g\chi^1|H_{\underline{q}}|\phi_g\chi^0\rangle\} \right|^2 \times \delta(\omega_{\underline{q}} - \omega). \tag{4}$$

To see explicitly what the phonon dependence is, it is convenient to regroup the terms of H_Q into terms with the electronic coordinate transforming according to the representations of the cubic group:

$$H_Q = H_Q^0(A_{1g}) + H_Q^1(T_{1u}) + H_Q^2(E_g, T_{2g}) + \ldots\ldots \tag{5}$$

where

$$\begin{aligned} H_Q^0 &= \sum_{\ell\neq 0} e^2\, Z_\ell \frac{1}{|\underline{R}_\ell|} \\ H_Q^1 &= -\sum_{\ell\neq 0} e^2\, Z_\ell \frac{\underline{R}_\ell\cdot\underline{r}}{|\underline{R}_\ell|^3} \\ H_Q^2 &= \sum_{\ell\neq 0} e^2\, Z_\ell \frac{1}{2|\underline{R}_\ell|^5} \{3(\underline{R}_\ell\cdot\underline{r})^2 - \underline{r}^2\, \underline{R}_\ell^2\} \\ &= \sum_{\ell\neq 0} \frac{e^2\, Z_\ell}{2|\underline{R}_\ell|^5} [\tfrac{3}{2}(x^2 - y^2)(X_\ell^2 - Y_\ell^2) \\ &\quad + \tfrac{1}{2}(2z^2 - x^2 - y^2)(2Z_\ell^2 - X_\ell^2 - Y_\ell^2) \\ &\quad + 6(xyX_\ell Y_\ell + yzY_\ell Z_\ell + zxZ_\ell X_\ell)] \,. \end{aligned} \tag{6}$$

---

*These terms for the even-phonon sideband may also be obtained by the configurational coordinate approach, as done by Bron (1965).

In these expressions, $\underline{R}_\ell$ represents $\underline{R}_{L\kappa} + \underline{u}_{L\kappa} - \underline{u}_{01}$, and

$$\underline{R}_\ell = x_\ell \hat{\underline{i}} + y_\ell \hat{\underline{j}} + z_\ell \hat{\underline{k}},$$
$$\underline{r} = x\ \hat{\underline{i}} + y\ \hat{\underline{j}} + z\ \hat{\underline{k}}$$

with $(\hat{\underline{i}}, \hat{\underline{j}}, \hat{\underline{k}})$ a set of Cartesian unit vectors.

As was done for H_Q^1 in Chapter 4, the terms of H_Q can be expanded, keeping terms linear in $\underline{u}_{L\kappa} - \underline{u}_{01}$. These terms in the expansion of H_Q^2 can be identified with the third derivatives of Φ^C. Thus, for example, the coefficient of (x^2-y^2) becomes

$$\sum_{\substack{L\kappa \neq 01 \\ \alpha}} (\Phi^C_{xx\alpha}(00L;11\kappa) - \Phi^C_{yy\alpha}(00L;11\kappa))(\underline{u}_{L\kappa\alpha} - \underline{u}_{01\alpha})$$

$$= \sum_{L\kappa\alpha} (\Phi^C_{xx\alpha}(00L;11\kappa) - \Phi^C_{yy\alpha}(00L;11\kappa))\ \underline{u}_{L\kappa\alpha} \qquad (7)$$

$$= \frac{1}{\sqrt{N}} \sum_{qj} \sum_{\kappa\alpha} \{\sum_{L} (\Phi^C_{xx\alpha}(00L;11\kappa) - \Phi^C_{yy\alpha}(00L;11\kappa))$$
$$\times \exp(i\underline{q}\cdot\underline{R}_{L\kappa})\} \ \frac{\xi_\alpha(\kappa\underline{q}j)}{\sqrt{M\kappa}}\ Q_{\underline{q}j};$$

the terms in $\underline{u}_{01}$ do not enter as the third derivatives are odd in at least one Cartesian coordinate and thus

$$\sum_{L'} \Phi^C_{\alpha\beta\gamma}(LLL';\kappa\kappa\kappa') = 0 \text{ for any } \alpha,\beta,\gamma.$$

Here,

$$\Phi^C_{xx\alpha}(00L;11\kappa) = \frac{\partial^3}{\partial u_{01x}\ \partial u_{01x}\ \partial u_{L\kappa\alpha}} (\Phi^C)]_{\underline{R}_0} \ ; \qquad (8)$$

the subscript $\underline{R}_o$ again indicates that the derivative is to be evaluated at the equilibrium positions.

Thus H_Q^2 can be rewritten

$$H_Q^2 = \sum_{\underline{q}j} \{A_{\underline{q}j}(x^2-y^2) + A'_{\underline{q}j}(2z^2-x^2-y^2) + B^1_{\underline{q}j}(xy)+B^2_{\underline{q}j}(yz)+B^3_{\underline{q}j}(zx)\}Q_{\underline{q}j}, \tag{9}$$

where $A_{\underline{q}j}$ is given by equation 7, and the other coefficients $A'_{\underline{q}j}$, $B^1_{\underline{q}j}$, and so on, are defined similarly. $A_{\underline{q}j}$ and $A'_{\underline{q}j}$ transform under operations on $\underline{R}$ like the rows of the E_g representation, while $B^1_{\underline{q}j}$, $B^2_{\underline{q}j}$, $B^3_{\underline{q}j}$ transform like the rows of the T_{2g} representation.

The problem is now greatly simplified; for equation 4 gives:

$$W_{e\to g}(\omega) = \frac{2\pi}{h} \sum_{\substack{\text{final}\\ \text{states}\\ \{p,q\}}} \frac{|\langle\phi_g|H_p|\phi_e\rangle\langle\chi^1|H_q|\chi^0\rangle|^2}{\hbar\omega_{\underline{q}}} \tag{10}$$

$$\times \; |A_{\underline{q}j}a + A'_{\underline{q}j}a' + B^1_{\underline{q}j}b^1 + B^2_{\underline{q}j}b^2 + B^3_{\underline{q}j}b^3|^2 \; \delta(\omega_{\underline{q}j} - \omega),$$

where constants have been defined:

$$a = \langle\phi_e|x^2 - y^2|\phi_e\rangle - \langle\phi_g|x^2 - y^2|\phi_g\rangle, \text{ etc.}$$

The phonon-dependent factor in Equation 10 is however, just proportional to $\sum_{\underline{q}j} (A_{\underline{q}j}^{\;2} + c\, B_{\underline{q}j}^{\;2})$, where c is a new constant, since

$$\sum_{\underline{q}j} A_{\underline{q}j}{}^2 = \sum_{\underline{q}j} A'_{\underline{q}j}{}^2 \text{ and } \sum_{\underline{q}j} B^1_{\underline{q}j}{}^2 = \sum_{\underline{q}j} B^2_{\underline{q}j}{}^2 = \sum_{\underline{q}j} B_{\underline{q}j}{}^2,$$

while $\sum_{\underline{q}j} A_{\underline{q}j} A'_{\underline{q}j}$, $\sum_{\underline{q}j} A_{\underline{q}j} B^1_{\underline{q}j}$, etc., are all zero as the two factors belong to different rows of the cubic representations.

Similarly, of course, the perturbed lattice problem completely uncouples for cubic symmetry, and one finds that the vectors $V_{\ell ka}$ analogous to those of the samarium problem have E_g, E'_g, T^1_{2g} etc. symmetry in (ℓka), and in the space where $\underline{\underline{T}}$ is block diagonal, will couple only to one block of $\underline{\underline{T}}$.

Note that under the assumptions made for the samarium problem, the A_{1g} symmetry term, H^0_Q, does not enter; for its contribution is proportional to $|\langle\phi_g|\phi_g\rangle - \langle\phi_e|\phi_e\rangle| = 0$. Also, for a perturbation model as taken for Sm^{++}, the T_{2g} modes are not perturbed; the unperturbed terms alone enter. Thus, as the coupling is much more short range than that for the samarium problem, one would expect that the sideband would be dominated by the perturbed E_g motions of the first neighbours of the impurity.

The low frequency ω-dependence predicted by this transition probability can be found as for the samarium problem. Here, for E_g terms,

$$W(\omega) \propto \frac{1}{\omega^2} \sum_{\underline{q}j} \{ \sum_{L\kappa\alpha} (\Phi^C_{xx\alpha}(0L;1\kappa) - \Phi^C_{yy\alpha}(0L;1\kappa))\exp(i\underline{q}\cdot\underline{R}_{L\kappa})$$

$$\times\ \xi_\alpha(\kappa\underline{q}j)\}^2\ \frac{\delta(\omega_{\underline{q}j}-\omega)}{\omega}$$

$$= \frac{1}{\omega^2}\sum_{\underline{q}j}\ \{\sum_{L\kappa\alpha}\ (\Phi^{C}_{xx\alpha}(0L;1\kappa)\ -\Phi^{C}_{yy\alpha}\ (0L;1\kappa))\sin(\underline{q}\cdot\underline{R}_{L\kappa})$$

$$\times\ \xi_\alpha(\kappa\underline{q}j)\}^2\ \frac{\delta(\omega_{\underline{q}j}-\omega)}{\omega}$$

$$\propto \omega. \qquad (11)$$

Here the first factor $(1/\omega^2)$ comes from the energy denominator in the transition probability, while at low ω, $\omega_{\underline{q}j} = v_j\, q$ and the density of states is proportional to ω^2.

This low frequency behaviour corresponds exactly to that observed for both $CaF_2:Eu^{++}$ (Hobden 1965) and $CaF_2:Sm^{++}$ (Kaiser et al. 1961); the sideband rises linearly with ω for about 150 cm^{-1} (see figure 15).

In general, however, the calculation of sidebands of allowed transitions is much more complicated than that of sidebands of forbidden transitions: for many more terms enter, forcing one to fit arbitrary constants to experiment; while the shorter range nature of the coupling makes the choice of $\underline{\Gamma}$ much more critical. Even for a cubic environment, A_{1g} terms may enter, as well as E_g and T_{2g}, if the approximation $\phi(\underline{r},\underline{R}) = \phi(\underline{r},\underline{R}_0)$ is not good. In this case one would have to calculate the A_{1g} contribution due to shells of neighbours and fit with arbitrary constants.

Figure 15. The sideband on the long-wavelength side of the 7082 Å transition ($4f^5 5d \rightarrow 4f^6$) transition of Sm^{++} in CaF_2. The correction for the photomultiplier response is not made. The sideband, corrected for the response of the photomultiplier, rises linearly up to about 150 cm^{-1}.

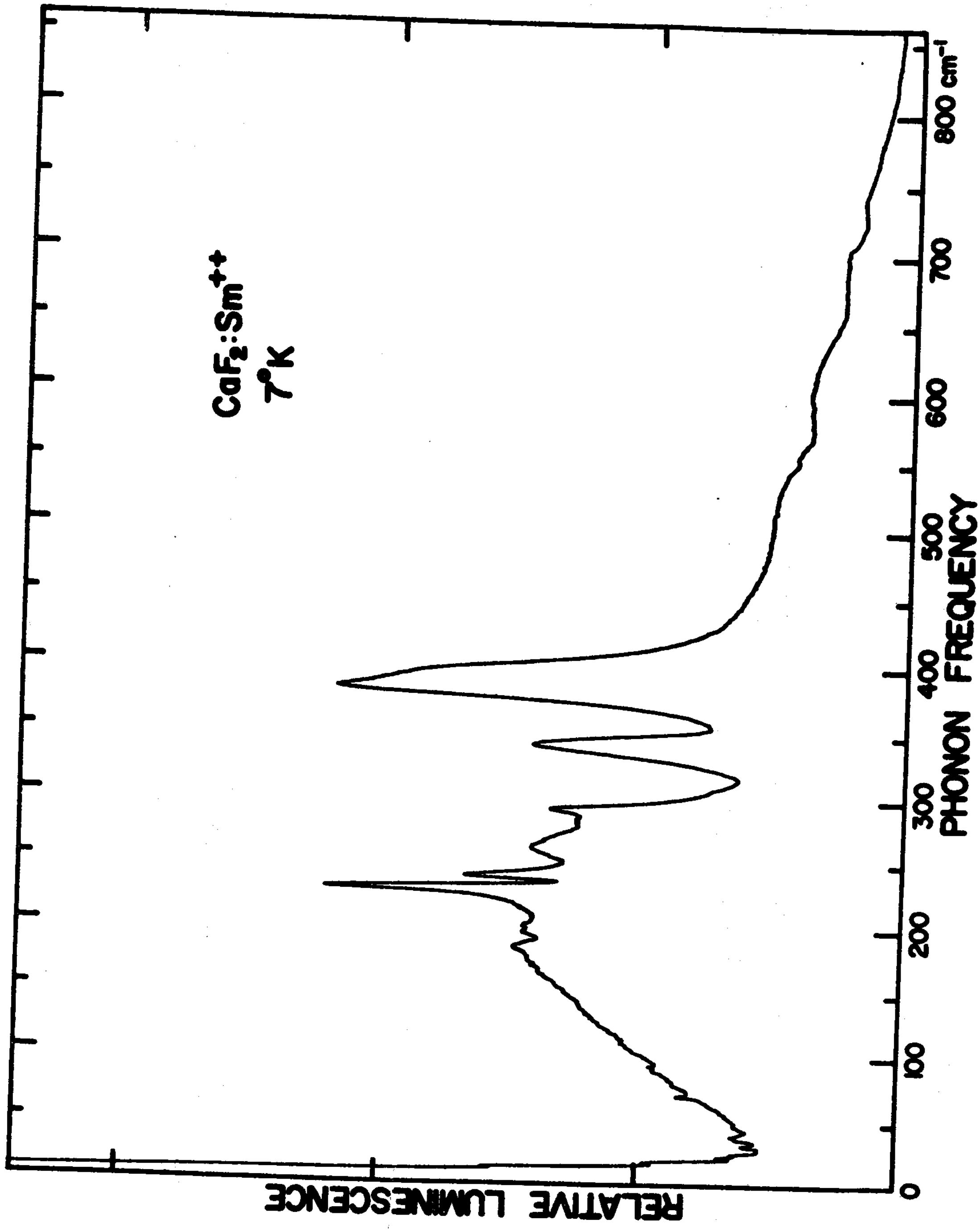
CaF$_2$:Sm^{++}
7°K
0
100
200
300
400
500
600
700
800 cm^{-1}
PHONON FREQUENCY
RELATIVE LUMINESCENCE

For the problem of Eu^{++}-doped alkali halides, the charge compensating vacancy may bring in terms of T_{1u} symmetry by mixing in electronic states of opposite parity. These T_{1u}-symmetry terms may not be negligible, since the long-range nature of the coupling makes H_Q^1 large. One is thus faced with the problem of a calculation involving a large number of unknown constants, corresponding to the ratios of the various contributions of different symmetry, as well as the force-constant changes.

Inspection of the $KBr:Eu^{++}$ and $KCl:Eu^{++}$ sideband spectra (figures 7 and 8) reveals several weak features characteristic of the perfect lattice. The peaks B and C of the $KBr:Sm^{++}$ spectrum agree in frequency with similarly shaped features in the $KBr:Eu^{++}$ curve. The rounded peak at 39 cm^{-1} (A') and the peak at 106 cm^{-1} (D') differ in frequency from peaks A and D, and are thus probably due to perturbed modes. The strong peak at 119 cm^{-1} agrees in frequency with the $KBr:Sm^{++}$ peak to the accuracy of these measurements, but may also be a perturbed mode. The rounded feature at the frequency of the peak F in $KBr:Sm^{++}$ is probably basically a two-phonon peak, corresponding to A' + D'.

For $KCl:Eu^{++}$, peaks are observed at the same frequencies as peaks B, C and D of the $KCl:Sm^{++}$ spectrum. The peak at 46 cm^{-1} and that at 197 cm^{-1} are at completely different frequencies from peaks observed in $KCl:Sm^{++}$, and are again expected to arise from perturbed modes.

In both cases, the peaks assigned to perturbed modes in the spectra of samarium-doped crystals do not appear, but are replaced by strong features at different frequencies, while the peaks assigned in the spectra of samarium-doped crystals to features in the density of states for the perfect crystal again appear but as very weak features.

A calculation was made of the perturbed E_g motions of the first neighbours on the model for $\underline{\underline{\Gamma}}$ discussed for Sm^{++}. This did not give the correct resonance frequencies for either KCl or KBr. It thus appears that the model for $\underline{\underline{\Gamma}}$ is not a sufficiently accurate description of the local environment for the calculation of these sidebands with more short range coupling. The weak features characteristic of the pure crystal may arise from an admixture of odd modes as a result of the charge compensating vacancy, or may in part be due to the effect of more distant ions in the transition probability for even modes.

The low frequency ω-dependence is much more difficult to determine for these sidebands than for CaF_2, where the dispersion curves are linear for more than 100 cm^{-1} (Cribier 1962) or for the samarium-doped crystals, where the zero-phonon line is quite narrow. Here, the zero-phonon line has a half-width of more than 5 cm^{-1}, and the first peak occurs at quite low frequency. It appears possible, however, that the curves are initially rising linearly with ω as expected for even-phonon sidebands.

CHAPTER 6

CONCLUSIONS

A combination of detailed experimental work and numerical calculations has shown that the sidebands observed in emission on the long-wavelength side of the $^5D_0 \rightarrow {}^7F_0$ transition of samarium in KBr and KCl reflect mainly the phonons of the perfect crystal. Singular points characteristic of the density of states are observed in the sideband spectra, and some regions are modified by resonances arising from the perturbation of the lattice by the impurity ion. The sideband has been shown to arise as a result of a Coulomb coupling between lattice and impurity. The small discrepancies between the experimental and the predicted sidebands have been assigned to the simplicity of the model for the perturbation of the lattice or to the shell model data used for the calculations. In particular, the frequencies of several Van Hove singularities which were directly observed were found to differ from those predicted by the shell model by as much as 6%.

APPENDIX A

TRANSFORMATION TO CUBIC DEFECT SPACE

The perturbed lattice problem is most simply treated by performing a transformation of coordinates from the space spanned by the displacements of the ions in the "defect space" to a space spanned by combinations of these displacements which transform according to the representations of the cubic group. This transformation will be written $\underline{\underline{\mathcal{D}}}$. In this "cubic" defect space, the matrix $\underline{\underline{\Gamma}}$ as well as the matrix $\underline{\underline{G}}^{\circ}$ becomes block diagonal; for the elements of these matrices are scalars and hence have A_{1g} symmetry; and in the cubic space they become

$$\langle \mathcal{D}(\Gamma_j^i)|M(A_{1g})|\mathcal{D}^{-1}(\Gamma_{j'}^{i'})\rangle, \qquad (1)$$

writing explicitly the symmetries of the transformation matrices $\mathcal{D}$ and of the matrix element M; $\mathcal{D}(\Gamma_j^i)$ transforms according to the i^{th} row of the representation Γ_j. This matrix element will be zero unless $j = j'$ and $i = i'$.

The $\underline{\underline{\Gamma}}$ matrix discussed in Chapter 4 has the block form:

$$\begin{bmatrix} \underline{\underline{\gamma}}(T_{1u}{}^{x}) & 0 & 0 & 0 & 0 & 0 \\ 0 & \underline{\underline{\gamma}}(T_{1u}{}^{y}) & 0 & 0 & 0 & 0 \\ 0 & 0 & \underline{\underline{\gamma}}(T_{1u}{}^{z}) & 0 & 0 & 0 \\ 0 & 0 & 0 & \underline{\underline{\gamma}}(A_{1g}) & 0 & 0 \\ 0 & 0 & 0 & 0 & \underline{\underline{\gamma}}(E_{g}) & 0 \\ 0 & 0 & 0 & 0 & 0 & \underline{\underline{\gamma}}(E_{g}{}') \end{bmatrix} \qquad (2)$$

in this space, where $\underline{\underline{\gamma}}(T_{1u}{}^{\alpha})$ is a 3×3 matrix, the same for all α, and $\underline{\underline{\gamma}}(A_{1g})$ and $\underline{\underline{\gamma}}(E_g) \equiv \underline{\underline{\gamma}}(E_g{}')$ are 2×2 matrices.

The transformation $\underline{\underline{\mathcal{D}}}$ that puts $\underline{\Gamma}$ and $\underline{\underline{G}}^{\circ}$ in block diagonal form is most easily written by considering its effect on the vector $\{u_{\ell ka}\}$, whose elements span the defect space. These elements will be written u_{2x}, u_{1x}, u_{0x}, $u_{\bar{1}x}$, etc., as was done for the vector $\{V_{\ell ka}\}$ in Chapter 4. The set then is $\{u_{n\alpha}\}$ with $n = 2, 1, 0, \bar{1}, \bar{2}$; and $\alpha = x, y, z$.

It is most convenient to define $\underline{\underline{\mathcal{D}}}$ in two parts: $\underline{\underline{\mathcal{D}}} = \underline{\underline{\mathcal{D}}}_1 \underline{\underline{\mathcal{D}}}_2$. Then

$$\underline{\underline{\mathcal{D}}}_1 \; \underline{u} = \begin{bmatrix} \underline{\underline{d}}_1 & 0 & 0 \\ 0 & \underline{\underline{d}}_1 & 0 \\ 0 & 0 & \underline{\underline{d}}_1 \end{bmatrix} \begin{bmatrix} \underline{u}_{nx} \\ \underline{u}_{ny} \\ \underline{u}_{nz} \end{bmatrix} \qquad (3)$$

where $n = 2, 1, 0, \bar{1}, \bar{2}$, and where $\underline{\underline{d}}_1$ is a 5×5 matrix:

$$\underline{\underline{d}}_1 = \begin{bmatrix} 1/\sqrt{2} & 0 & 0 & 0 & 1/\sqrt{2} \\ 0 & 1/\sqrt{2} & 0 & 1/\sqrt{2} & 0 \\ 0 & 0 & 1 & 0 & 0 \\ 0 & 1/\sqrt{2} & 0 & -1/\sqrt{2} & 0 \\ 1/\sqrt{2} & 0 & 0 & 0 & -1/\sqrt{2} \end{bmatrix} \quad ; \quad (4)$$

and

$$\underline{\underline{d}}_1\ \underline{u}_{nx} = \begin{bmatrix} (u_{2x} + u_{\bar{2}x})/\sqrt{2} \\ (u_{1x} + u_{\bar{1}x})/\sqrt{2} \\ u_{0x} \\ (u_{1x} - u_{\bar{1}x})/\sqrt{2} \\ (u_{2x} - u_{\bar{2}x})/\sqrt{2} \end{bmatrix} \equiv \begin{bmatrix} u_{2x}^{o} \\ u_{1x}^{o} \\ u_{0x}^{o} \\ u_{1x}^{e} \\ u_{2x}^{e} \end{bmatrix} \quad , \quad (5)$$

where the first three elements, u_{2x}^{o}, u_{1x}^{o}, u_{0x}^{o} have odd parity and are of $T_{1u}{}^{x}$ symmetry, and the last two u_{1x}^{e}, u_{2x}^{e} have even parity.

The matrix $\underline{\underline{\mathcal{D}}}_2$ is defined such that

$$\underline{\underline{\mathcal{D}}}_2(\underline{\underline{\mathcal{D}}}_1\underline{u}) = \begin{bmatrix} \underline{\underline{I}} & 0 & 0 & 0 & 0 \\ 0 & \underline{\underline{I}} & 0 & 0 & 0 \\ 0 & 0 & \underline{\underline{I}} & 0 & 0 \\ 0 & 0 & 0 & \underline{\underline{d}}_2 & 0 \\ 0 & 0 & 0 & 0 & \underline{\underline{d}}_2 \end{bmatrix} \begin{bmatrix} \underline{u}_{nx}^{o} \\ \underline{u}_{ny}^{o} \\ \underline{u}_{nz}^{o} \\ \underline{u}_{1}^{e} \\ \underline{u}_{2}^{e} \end{bmatrix} \quad , \quad (6)$$

where each submatrix is 3×3 , the elements of $(\underline{\underline{\mathcal{D}}}_1\underline{u})$ have been re-ordered for convenience and

$$\underline{\underline{d}}_2\, \underline{u}_1{}^e = \begin{bmatrix} 1/\sqrt{3} & 1/\sqrt{3} & 1/\sqrt{3} \\ 1/\sqrt{2} & -1/\sqrt{2} & 0 \\ 1/\sqrt{6} & 1/\sqrt{6} & -2/\sqrt{6} \end{bmatrix} \begin{bmatrix} u_{1x}^e \\ u_{1y}^e \\ u_{1z}^e \end{bmatrix}$$

$$= \begin{bmatrix} (u_{1x}^e + u_{1y}^e + u_{1z})/\sqrt{3} \\ (u_{1x}^e - u_{1y}^e)/\sqrt{2} \\ (u_{1x}^e + u_{1y}^e - 2u_{1z}^e)/\sqrt{6} \end{bmatrix} \quad . \quad (7)$$

Here the first element of ($\underline{\underline{d}}_2\, \underline{u}_{1x}^e$) has A_{1g} symmetry, the second E_g symmetry, and the third $E_g{}'$ symmetry.

The transformations for more extensive defect spaces can be found straightforwardly by forming the appropriate linear combinations of the set $u_{\ell ka}$.

APPENDIX B

EVALUATION OF V AND G° USING SOLUTIONS IN $1/48^{th}$ OF THE BRILLOUIN ZONE

The set of normal mode solutions to the unperturbed lattice problem are usually given only for the "irreducible $1/48^{th}$" of the Brillouin zone, since the solutions for the rest of the Brillouin zone may be found from them by operating with all 48 symmetry operations of the cubic group. Thus, the sums over $\{qj\}$ involved in the evaluation of the $\underline{\underline{G}}^{\circ}$'s and $\underline{V}$'s must be performed in two parts: the sum over all $\underline{q}$'s that are equivalent by symmetry must be done explicitly, followed by the summation $\sum'_{\underline{q}}$ over the solutions in the irreducible $1/48^{th}$. The resultant function will have full cubic symmetry: it will be even in q_x, q_y, and q_z, and the three coordinates will appear in a completely symmetric way.

To apply this, one must know how the various functions of $\underline{q}$ and $\underline{R}$ behave under all rotations and reflections consistent with cubic symmetry. The eigenvectors $\underline{\xi}(\kappa\underline{q}j)$ are taken to transform as the vector $\underline{q}$ does. (One may assume either $\underline{\xi}(\underline{q}) = +\,\underline{\xi}(-\underline{q})$ or $\underline{\xi}(\underline{q}) = -\,\underline{\xi}(-\underline{q})$; the second is taken, as being more physical).

This is most easily illustrated by a diagram:

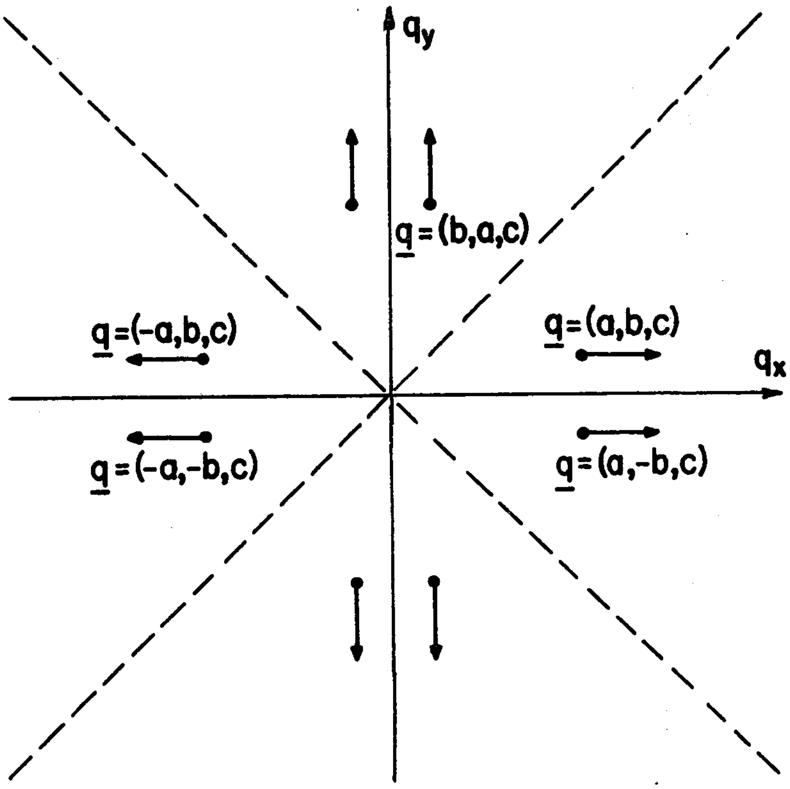

The diagram represents the plane $q_z = c$ through the Brillouin zone. The points indicated on it represent a set of $\underline{q}$ values related to each other by cubic symmetry operations. The solid and dashed lines are mirror planes. The arrows represent components of the eigenvectors $\underline{\xi}(q_x, q_y, q_z)$ that are equal to each other as a result of the symmetry. Thus,

$$\xi_x(a,b,c) = \xi_y(b,a,c) \tag{1}$$

while

$$\begin{aligned} \xi_x(a,b,c) &= \xi_x(a,-b,c) \\ &= -\xi_x(-a,b,c) \\ &= -\xi_x(-a,-b,c), \text{ etc.} \end{aligned} \tag{2}$$

Similarly, the force constants $\Phi_{\alpha\beta}(LL';\kappa\kappa')$ transform like the dyadic $\underline{R}\underline{R}$, where $\underline{R} = \underline{R}_{L\kappa} - \underline{R}_{L'\kappa'}$. Again the

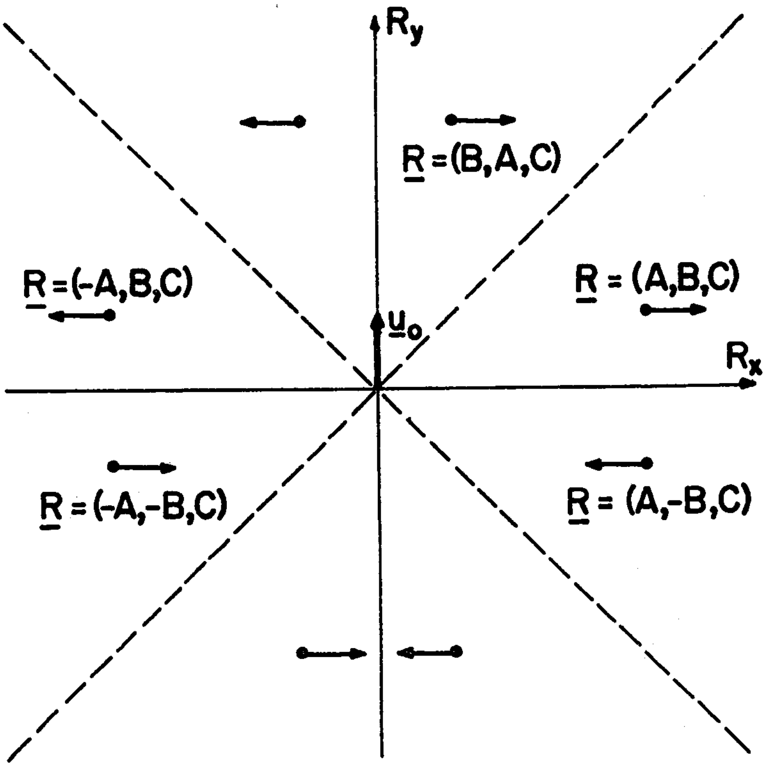

diagram represents the $R_z = C$ plane, and the points represent ions at $\underline{R} = (R_x, R_y, R_z)$, whose positions are related by symmetry operations. The arrows from these points represent the magnitude and direction of the forces on these ions when the ion at the origin is displaced by $\underline{u}_o$. The size and sign of these vectors is then proportional to the force constant $\Phi_{xy}(\underline{R})$. Thus,

$$\begin{aligned} \Phi_{xy}(A,B,C) &= -\Phi_{xy}(A,-B,C) \\ &= -\Phi_{xy}(-A,B,C) \qquad (3) \\ &= \Phi_{xy}(-A,-B,C), \text{ etc.} \end{aligned}$$

and

$$\Phi_{xy}(A,B,C) = \Phi_{xy}(B,A,C); \text{ etc.} \qquad (4)$$

The following diagram represents the relationship between the two force constants $\Phi_{xy}(A,B,C)$, corresponding to the solid line vectors, and $\Phi_{yx}(B,A,C)$, corresponding to the dashed vectors:

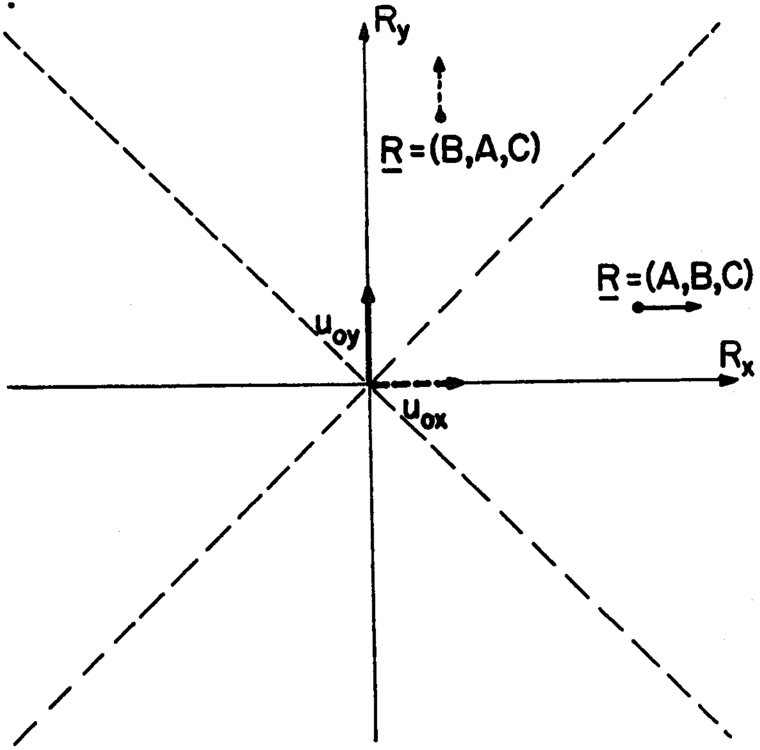

Obviously, $\Phi_{xy}(A,B,C) = \Phi_{yx}(B,A,C)$; (5)

and it follows, from similar diagrams, that:

$$\Phi_{xy}(A,B,C) = \Phi_{xz}(A,C,B) \qquad (6)$$

and so on. Also, comparing equations (4) and (5), one has

$$\Phi_{xy}(A,B,C) = \Phi_{yx}(A,B,C) . \qquad (7)$$

It follows from these results that the Coulomb coefficients transform like the dyadic $\underline{q}\underline{q}$. For example, writing $C\left(\begin{matrix}\kappa\kappa'\\ \alpha\beta\\ \underline{q}\end{matrix}\right)$ as $C_{\alpha\beta}(\underline{q})$, then

$$C_{xy}(a,b,c) = C_{xz}(a,c,b). \tag{8}$$

For consider

$$C_{xy}(\underline{q}) = \sum_{R} \Phi_{xy}(\underline{R}) \exp(i\underline{q}\cdot\underline{R})$$

for q = (a,b,c). Writing the two terms in this sum which correspond to $\underline{R}_1 = (A,B,C)$ and $\underline{R}_2 = (A,C,B)$ gives

$$\begin{aligned}&\Phi_{xy}(A,B,C)\ \exp(i(aA+bB+cC)) + \Phi_{xy}(A,C,B)\ \exp(i(aA+bC+cB))\\ \equiv\ &\Phi_{xz}(A,C,B)\ \exp(i(aA+bB+cC)) + \Phi_{xz}(A,B,C)\ \exp(i(aA+bC+cB));\end{aligned} \tag{9}$$

but these are the terms corresponding to $\underline{R}_2$ and $\underline{R}_1$ in the expansion of $C_{xz}(a,c,b)$.

Using these results one can write down explicitly the expressions for $\underline{\underline{G}}^\circ$ and $\underline{\underline{V}}$ in terms of their values in the irreducible 1/48th. For example, the element of $\underline{\underline{G}}^\circ$ corresponding to the ion of type 2 at $\underline{R}_{L\kappa} = (a/2)\hat{\underline{i}}$, moving in the x direction ($L\kappa\alpha=1x$), and that of type 1 at $\underline{R}_{L'\kappa'} = a\hat{\underline{i}}$ moving in the x direction ($L'\kappa'\beta= 2x$) is:

$$\begin{aligned}G^\circ_{1x,2x}(\omega) &= \frac{1}{N}\sum_{\underline{q}j} \frac{\xi_x(1\underline{q}j)\ \xi_x(2\underline{q}j)}{\omega_{\underline{q}j}^{\ 2} - \omega^2}\ \exp\{i\underline{q}\cdot((a/2)\hat{\underline{i}}-a\hat{\underline{i}})\}\\ &= \frac{1}{N}\sum_{\underline{q}j} \frac{\xi_x(1\underline{q}j)\ \xi_x(2\underline{q}j)}{\omega_{\underline{q}j}^{\ 2} - \omega^2}\ \exp(-iq_x a/2)\end{aligned}$$

$$= \frac{8}{N} \sum_{\underline{q}j}{}' \Big[[\xi_x(1\underline{q}j)\ \xi_x(2\underline{q}j)(\exp(-iq_x a/2) + \exp(+iq_x a/2)$$

$$+ \xi_y(1\underline{q}j)\ \xi_y(2\underline{q}j)(\exp(-iq_y a/2) + \exp(+iq_y a/2)) \qquad (10)$$

$$+ \xi_z(1\underline{q}j)\ \xi_z(2\underline{q}j)(\exp(-iq_z a/2) + \exp(+iq_z a/2)\Big] \times \frac{1}{\omega_{\underline{q}j}^{2} - \omega^2}$$

where $\underline{q}$ now runs over only 1/48th : forty-eight terms have been written explicitly. Here, the first eight terms, $[8\xi_x(1)\ \xi_x(2)\ \exp(-iq_x a/2)]$, correspond to the sets $\{q_x,\ \pm q_y,\ \pm q_z\}$ and $\{q_x,\ \pm q_z,\ \pm q_y\}$ in the full zone; the second eight terms, to the sets $\{-q_x,\ \pm q_y,\ \pm q_z\}$ and $\{-q_x,\ \pm q_z,\ \pm q_y\}$; the third, to $\{q_y,\ \pm q_z,\ \pm q_x\}$ and $\{q_y,\ \pm q_x,\ \pm q_z\}$; and so on. Equation (10) in simplest form is

$$G^{\circ}_{1x,2x}(\omega) = \frac{16}{N} \sum_{\substack{\underline{q}j \\ \alpha}}{}' \xi_\alpha(1\underline{q}j)\ \xi_\alpha(2\underline{q}j)\ \cos(q_\alpha a/2). \qquad (11)$$

Similarly $V_{\ell ka}$ for $k = 2$, $\underline{R}_{\ell k} = (a/2)\hat{\underline{i}}$ is:

$$V_{1x} = \frac{1}{N} \sum_{\underline{q}j} \sum_{\kappa\alpha} C^{1\kappa}_{\underline{q}}(x\alpha)\ \xi_\alpha(\kappa\underline{q}j)\ \xi_x(2\underline{q}j)\ \exp(-iq_x a/2)$$

$$= \frac{1}{N} \sum_{\underline{q}j} \sum_{\kappa\alpha} C^{1\kappa}_{\underline{q}}(x\alpha)\ \xi_\alpha(\kappa\underline{q}j)\ \xi_x(2\underline{q}j)\ \cos(q_x a/2)$$

(making the function even in x)

$$= \frac{16}{N} \sum_{\substack{\underline{q}j \\ \beta}}{}' \sum_{\kappa\alpha} C^{1\kappa}_{\underline{q}}(\beta\alpha)\ \xi_\alpha(\kappa\underline{q}j)\ \xi_\beta(2\underline{q}j)\ \cos(q_\beta a/2) \qquad (12)$$

(summing over the 48 symmetry-related $\underline{q}$'s). For k=2,

$\underline{R}_{\ell k} = (a/2)\hat{\underline{j}}$, $V_{\ell ka}$ is:

$$V_{1y} = \frac{1}{N} \sum_{\underline{q}j} \sum_{\kappa\alpha} C\overset{1\kappa}{\underset{\underline{q}}{(x\alpha)}}\ \xi_{\alpha}(\kappa\underline{q}j)\ \xi_{y}(2\underline{q}j)\ \exp(-iq_{y}a/2)$$

$$= \frac{1}{N} \sum_{\underline{q}j} \sum_{\kappa\alpha} C\overset{1\kappa}{\underset{\underline{q}}{(x\alpha)}}\ \xi_{\alpha}(\kappa\underline{q}j)\ \xi_{y}(2\underline{q}j)\ \sin(q_{y}a/2). \qquad (13)$$

This function is even in α and y, but is odd in x; therefore performing the sum over all symmetry related $\underline{q}$'s, the terms with the $q_x = +a$ and those with $q_x = -a$ cancel; so

$$V_{1y} = V_{1z} \equiv 0 \quad . \qquad (14)$$

APPENDIX C

MECHANISM FOR COUPLING TO THE LATTICE OF BRON

The coupling mechanism proposed by Bron (1965) depends on there being a strong field from the vacancy, so that odd parity electronic states are mixed in by this field rather than the odd parity phonon field. Secondly, he does not neglect the dependence of the lattice state χ_n^n on the electronic wave function, but handles these matrix elements by the "configurational coordinate" approach. In addition, all Bron's discussions are carried out assuming a vacancy at $(\frac{a}{2},\frac{a}{2},0)$, which may not be a good approximation, as has been discussed.

In his approach, the transition probability for the sideband is proportional to the square of the matrix element

$$<\psi_g|H_p|\psi_e> = <\Phi_g|H_p|\Phi_e> <\chi_g^1(Q_\kappa^e - \alpha_\kappa^{ge})|\chi_e^0(Q_\kappa^e)> , \quad (1)$$

where the set $\{Q_\kappa\}$ are the nuclear normal modes and α_κ^{ge} is the change in the equilibrium position of the normal mode between the states g and e:

$$\alpha_\kappa^{ge} = \frac{1}{\omega_\kappa^2} \{<\Phi_g|U_\kappa|\Phi_g> - <\Phi_e|U_\kappa|\Phi_e>\}. \quad (2)$$

Here, H_Q has been written

$$H_Q = \sum_\kappa U_\kappa Q_\kappa . \qquad (3)$$

Also,

$$|\langle \chi_g^\eta (Q_\kappa^e - \alpha_\kappa^{ge}) | \chi_e^0 (Q^e) \rangle|^2 = \frac{1}{\eta !} \left[\frac{\omega_\kappa \alpha_\kappa^2}{2n}\right]^n . \qquad (4)$$

Thus, for Φ_g and Φ_e states of opposite parity, even phonons enter and this transition probability gives identical terms to those obtained in Chapter 5.

For a transition between states of the same parity, Bron writes

$$\Phi_n = a_n \phi_n - \sum_i \frac{\langle \phi_i | H_s | \phi_n \rangle}{\varepsilon_i - \varepsilon_n} \phi_i ; \qquad (5)$$

H_s is the vacancy Hamiltonian, and the state ϕ_i is of opposite parity from ϕ_n. Equation 2 then gives

$$\omega_\kappa^2 \alpha_\kappa^{ge} = a_g^2 \langle \phi_g | U_\kappa | \phi_g \rangle - a_e^2 \langle \phi_e | U_\kappa | \phi_e \rangle$$

$$- a_g \sum_i \frac{\langle \phi_i | H_s | \phi_g \rangle \langle \phi_g | U_\kappa | \phi_i \rangle}{\varepsilon_i - \varepsilon_g} - a_e \sum_i \frac{\langle \phi_i | H_s | \phi_e \rangle \langle \phi_e | U_\kappa | \phi_i \rangle}{\varepsilon_i - \varepsilon_e} . \qquad (6)$$

Since ϕ_g and ϕ_e are of even parity, and ϕ_i of odd parity, the first two terms on the right hand side of equation 6 give a coupling to even phonons, and the last two a coupling to odd phonons. For $^5D_0$ and $^7F_0$ states, the only even terms that could enter are those of A_{1g} symmetry since the wave functions have A_{1g} symmetry; but these terms, as discussed in Chapter 5, are zero in this approximation.

The terms corresponding to odd-parity phonons give the same projection as does the calculation of $W^\circ(\omega)$, but with an additional $1/\omega^2$ factor. The sideband predicted by this mechanism, then,has a different frequency dependence for low ω from that observed experimentally, as well as predicting much lower intensity in the optical branch.

In addition, the configurational coordinate picture predicts a definite ratio for $I_0 : I_1 : I_2$, where I_2 is the total intensity of the two-phonon sideband. For, writing $\frac{\omega_\kappa \alpha_\kappa^2}{2h}$ as s,

$$I_0 : I_1 : I_2 = 1 : s : s^2/2. \qquad (7)$$

The ratio I_1/I_0 has been determined to 0.4, and the low continuum beyond the one-phonon sideband permits one to put an upper limit on the two-phonon intensity. It appears that I_2 is much smaller ,by a factor of ten ,than that predicted by this mechanism.

It seems, then, that the mechanism of Bron does not explain the experimental results and must be less important than the terms used in this thesis.

BIBLIOGRAPHY

Ballhausen, Carl J. 1962. *Introduction to Ligand Field Theory* (McGraw-Hill, New York).

Bron, W. E., and Heller, W.R. 1964. Phys. Rev. *136*, A1433.

Bron, W. E. 1965. Phys. Rev. *140*, A2005.

Copley, J.R.D., MacPherson, R.W., and Timusk, T. To be published in the Physical Review.

Cowley, R. A., Cochran, W., Brockhouse, B.N., and Woods, A.D.B. 1963. Phys. Rev. *131*, 1030.

Cowley, E. R. and Cowley, R. A. 1966. Proc. Roy. Soc., Ser. A, *292*, 209.

Cribier, D., Farnoux, B., and Jacrot, B. 1962. In *Inelastic Scattering of Neutrons in Solids and Liquids* Vol. 2 (International Atomic Energy Agency, Chalk River, 1962), p. 225.

Davydov, A.S. 1966. *Quantum Mechanics* (NEO Press, Ann Arbour), p. 301. [Originally published in Russian by the Government Publishing House for Physical and Mathematical Literature (Fizmatgiz), Moscow, 1963].

Fong, Francis K. and Wong, Eugene Y. 1967. Phys. Rev. *162*,348.

Hobden, M.V. 1965. Phys. Letters *15*, 10.

Kaiser, W., Garrett, C.G. B., and Wood, D.L. 1961. Phys. Rev. *123*, 766.

Kaplyanskii, A. A. and Feofilov, P.P. 1964. Opt. i Spekstroscopiya 16, 264. [Eng. transl: Opt. Spectry. (USSR) 16, 144].

Kellermann, E. W. 1940. Phil. Trans. Roy. Soc. (London), 238,513.

Kittel, Charles. 1956. Introduction to Solid State Physics, Second edition (Wiley, New York), p. 160.

Klein, M.V. 1963. Phys. Rev. 131, 1500.

Klein, M.V. 1968. In Physics of Color Centres, edited by W. B. Fowler (Academic Press, New York).

McClure, Donald S. 1959. Solid State Physics, Vol. 9, edited by F. Seitz and D. Turnbull (Academic Press, New York).

Runciman, W. A. and Stager, C.V. 1962. J. Chem. Phys. 37, 196.

Runciman, W. A. and Stager, C.V. 1963. J. Chem. Phys. 38, 279.

Schiff, Leonard I. 1955. Quantum Mechanics, Second edition, (McGraw-Hill, New York) p. 201.

Timusk, T. and Klein, M.V. 1966. Phys. Rev. 141, 664.

Timusk, T. and Buchanan, M. 1967. Phys. Rev. 164, 345.

Wagner, Max and Bron, W.E. 1965. Phys. Rev. 139, A223.

Woll, E.J.,Jr., Gethins, T., and Timusk, T. 1968. Can. J. Phys. 46, 2263.

Woods, A.D.B., Brockhouse, B.N., Cowley, R.A., and Cochran, W. 1963. Phys. Rev. 131, 1025.